Study of the Optimized Parameters of Stainless Steel 316L Powder for Rapid Prototyping Based on Selective Laser Melting Technique

Apinya Laohaprapanon

A Thesis Submitted in Fulfillment of the Requirements for the Degree of

Master of Engineering in Materials Engineering

Prince of Songkla University

2011

Thesis Title	Study of the Optimized Parameters of Stainless Steel 316L Powder for Rapid Prototyping Based on Selective Laser Melting Technique
Author	Miss Apinya Laohaprapanon
Major Program	Materials engineering

Major Advisor	**Examining Committee:**
…….	...……...……..…… ….Chairperson
(Assoc. Prof. Dr. Sirikul Wisutmethangoon)	(Asst. Prof. Dr. Thawatchai Plookphol)
	……..……..……..……
Co-advisor	(Asst. Prof. Dr. Prapas Muangjunburee)
…….	…….……...…
(Dr. Kriskrai Sitthiseripratip)	(Dr. Prasert Chalermkarnnon)

The Graduate School, Prince of Songkla University, has approved this thesis as fulfillment of the requirements for the Master of Engineering Degree in Materials Engineering

..……..……

(Prof. Dr. Amornrat Phongdara)

Dean of Graduate School

ชื่อวิทยานิพนธ์	การศึกษาพารามิเตอร์ที่เหมาะสมของผงเหล็กกล้าไร้สนิมเกรด 316L สำหรับการขึ้นรูปต้นแบบรวดเร็วด้วยเทคนิค Selective Laser Melting
ผู้เขียน	นางสาว อภิญญา เลาหประภานนท์
สาขาวิชา	วิศวกรรมวัสดุ
ปีการศึกษา	2554

บทคัดย่อ

การศึกษานี้มีเป้าหมายเพื่อหาค่าตัวแปรที่เหมาะสมในการขึ้นรูปเหล็กกล้าไร้สนิมเกรด 316L ด้วยกระบวนการหลอมละลายด้วยเลเซอร์ (Selective Laser Melting, SLM) ซึ่งตัวแปรของการทดลองประกอบด้วย พลังงานเลเซอร์ (Laser power) ระหว่าง 25 W ถึง 225 W ความเร็วของการสแกน (Scanning speed) ระหว่าง 50 mm/s ถึง 320 mm/s ระยะห่างระหว่างรอยสแกน (Scan spacing) ที่ 0.04 mm และ 0.06 mm และ รูปแบบการสแกน (Scan strategy) เป็นการสแกนระยะ 5 mm (Sub-sector) และสแกนระยะ 10 mm (Without sub-sector) นอกจากนี้การทดลองจะทดลองที่ความหนาของชั้นผงโลหะ (Layer thickness) 100 μm และตัวแปรทั้งหมดจะถูกทำการทดลองภายใต้ 2 การทดลอง คือ การสแกนเป็นเส้นเดียว (Single line scanning) และการสแกนเป็นชิ้นงานสามมิติ (Multiple-layer scanning) สำหรับชิ้นงานของการสแกนเป็นเส้นเดียวนั้นจะถูกวิเคราะห์ด้วยตา และสำหรับการสแกนเป็นชิ้นงานสามมิตินั้น วิธีการวิเคราะห์ที่เรียกว่า 2^k แฟคทอเรียลถูกนำมาใช้เพื่อหาค่าตัวแปรที่เหมาะสม โดยการวัดค่าความหนาแน่น ความแข็ง และอัตราเร็วในการขึ้นรูปของชิ้นงาน จากการทดลองนี้พบว่าค่าตัวแปรของการทดลองที่เหมาะสม คือ พลังงานเลเซอร์ 175 W ความเร็วในการสแกน 200 mm/s ระยะห่างระหว่างรอยสแกน 0.04 mm และรูปแบบการสแกนเป็นระยะ 5 mm (Sub-sector) เมื่อขึ้นรูปชิ้นงานด้วยค่าตัวแปรที่เหมาะสมนี้จะได้ชิ้นงานที่มีความหนาแน่นเป็น 98.6% ความแข็ง 228±5 HV ความแข็งแรงดึง 474 MPa อัตราเร็วในการขึ้นรูป 1.87cm^3/hr และพบว่าโครงสร้างจุลภาคของชิ้นงานเป็นโครงสร้างเซลลูลาร์เดรนไดรต์

Thesis Title	Study of the Optimized Parameters of Stainless Steel 316L Powder for Rapid Prototyping Based on Selective Laser Melting Technique
Author	Miss Apinya Laohaprapanon
Major Program	Materials Engineering
Academic Year	2011

ABSTRACT

This study aims to determine optimal processing parameters for fabricating stainless steel 316L processing using selective laser melting (SLM) technique. The parameters under consideration include laser power (25-225 W), scanning speed (50-320 mm/s), scan spacing (0.04 and 0.06 mm) and scanning strategy (with and without sub-sector). In addition, the layer of stainless steel was kept always at the constant thickness of 100 μm. All parameters were analyzed based on two types of experiments i.e. single line scanning and multiple-layer scanning. For single line scanning, each of final parts was examined using only visual inspection. For multiple-layer scanning, the 2^k factorial analysis was used to optimize the parameters based on the measurement of density, Micro-hardness and build rate of each final part. From our experiments, it found that the optimal parameters were laser power 175 W, scan speed 200 mm/s, scan spacing 0.04 mm with scan sub-sector strategy. The parts processed using these optimal parameters reached 98.6% of density, 228±5 of HV hardness, 474 MPa of tensile strength and build rate 1.87cm^3/hr. Besides, it was found that the microstructure of part contained fine cellular dendrite grain structures.

ACKNOWLEDGEMENTS

This thesis completely, I would like to say grateful thank and deeply indebted to my thesis advisor, Asst. Prof. Dr. Sirikul Wisutmethangoon for guidance, encouragement and valuable advice for completely writing of thesis. I would like to thank Dr. Kriskrai Sitthiserripratip my co-advisor for valuable comments and suggestion.

Thanks my friends at Medical rapid prototyping laboratory, National Metal and Materials Technology Center (MTEC), and Mr. Pongnarin Jeamwatthanachai for their assistance. I would also like to thank the National Metal and Materials Technology Center (MTEC), Thailand for their kind support of providing the use of their facilities. I would like to thank Thailand Graduate Institute of Science and Technology (TGIST) for the scholarship.

Finally, I'm especially appreciated my family and my friends for their continuing encouragements and support.

Apinya Laohaprapanon

CONTENTS

Subject	Page

LIST OF TABLES

LIST OF FIGURES

LIST OF FIGURES (CONTINUED)

LIST OF FIGURES (CONTINUED)

Figure **Page**

CHAPTER 1

Introduction

1.1. Background of the study

Rapid Prototyping (RP) techniques were initially developed by Prof. Herbert Voelcker in late 1960s and in the 1980s, this technology became available and since then it has rapidly growth and known as a quickly fabricated a scale model or a part of assembly using three-dimension computer aided design (CAD) data and automated machines (Santos et al., 2006; Kruth et al., 2007). Initially, RP is mostly used to fabricate a prototype based on polymers for communication and inspection tools. Today, the application of RP is not just about prototyping but also included all applications of the technology such as pattern making, tool making, and the production of end-use parts in volumes of one to thousands or more (Kruth et al., 2010).

The working principle of all RP processes is mainly consist of 3 major steps (i) creation of a three-dimensional model using a computer (ii) process planner and (iii) layer deposition. As it is shown in Figure 1.1, the model is created from 3D CAD software program, data from 3D digitizing systems of from CT and MRI scans. Subsequently, this information is then sent to a computer program. The process planner decomposed the three-dimensional part into thin layers and generated the necessary deposition paths for each layer. This information was then sent to a deposition station, which built the part layer by layer to completion (Rombouts, 2006).

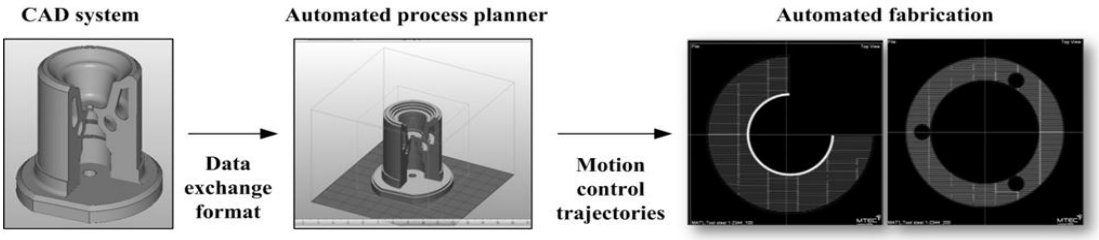

Figure 1.1: Rapid prototyping build process (Source: The National Metal and Materials Technology Center).

Many RP technologies are available nowadays as including (i) stereolithography (SLA) (ii) ink-jet printing (IJP) (iii) 3D-printing (3DP), (iv) selective laser sintering or melting (SLS/SLM) and etc.,. Fundamentally, the difference of these technologies is based on the materials for manufacturing and the consolidation mechanism during the process carry out. The latter determined the range of possible materials. Basic process principles of different RP technologies are briefly described as follows:

- **Ink jet printing (IJP)**

  The ink replaced with thermoplastic and wax materials, which were held in a melted state. When printed, liquid drops of these materials instantly cool and solidify to form a layer of the part (Ben, 2008).

- **3D-Printing (3D-P)**

  The solid powder material was deposited in layers that were successively solidified by inkjet printing droplets of binder onto the powder material. For materials can use polymers, ceramics and metals (Kruth, Leu, and Nakagawa, 1998)**.**

- **Stereolithography (SLA)**

  The liquid resin were consolidated and solidified when it was exposed to ultraviolet (UV) light. Due to the absorption and scattering of the laser beam which scanned selectively successive liquid layers. The materials photo-polymers based on acrylic or epoxy resins (Pham and Gault, 1998).

- **Selective laser sintering/melting (SLS/SLM)**

  Successive layers of powder material selective bound by fusing or sintering together of a laser beam. It mostly involved (partial) melting and resolidification by cooling. This process can fabricate ceramic, polymer parts and metals without binder (Kruth et al., 2007) (Ben, 2008)

- **Fused deposition modeling (FDM)**

  Material was fed through a heating element, which heated it to a semi-molten state. The filament was then fed through a nozzle and built up layer-wisely by continuous extrusion. Possible materials polymers like ABS (Sung-Hoon et al., 2002).

- **Laser cladding (LC)**

  The powder material sprayed through a nozzle into the spot of a laser beam focused on the workpiece, followed by solidification by cooling. Metals were used this process (Kruth, Leu, and Nakagawa, 1998).

- **Laminated object manufacturing (LOM)**

  The build material is applied to the part from a roll, and then bonded to each other. The contour of each layer was cut with a laser and then it was carefully modulated to penetrate to a depth of exactly one layer thickness. Materials of process were papers, polymers and metals (Pham and Gault, 1998).

The advantage of RP is the direct link between the CAD model and final part. Therefore, the new fabrication concept allows the building of complex parts starting from a 3D-CAD model without using a mould and mostly no tooling is involved, that reduced the total production time and cost. RP processes are also well suited for the fabrication of parts with customized features. Feed materials can be used by varying different materials during the building process (Ben, 2008). Figure 1.2 illustrates some examples products based on RP technologies.

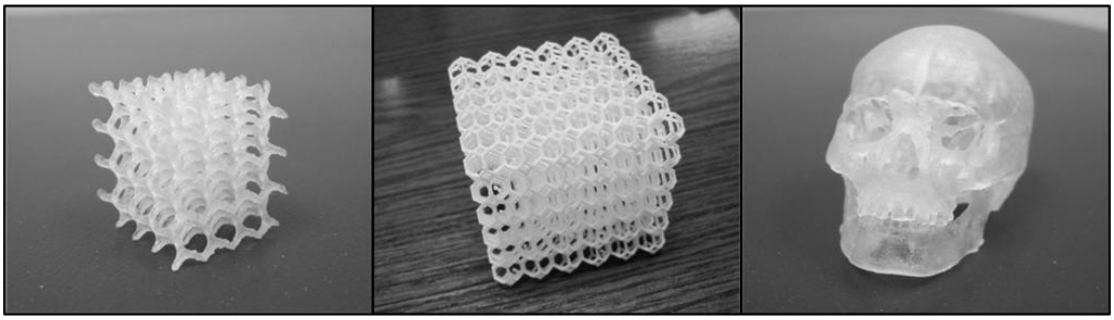

Figure 1.2: Examples of Rapid prototyping, showing geometrical freedom (Source: The National Metal and Materials Technology Center).

Selective laser melting

At present this reports is focused on selective laser melting (SLM) which is known as an additive manufacturing technology and originally comes from the technology development of rapid prototyping (RP). The process of SLM basically uses a high powered ytterbium fiber laser to melt and fuse metallic powders to form 3-dimentionsal parts directly from the CAD file data (Ben, 2008). The formation is based on means of adding layers to build net shape components. The consolidation is accomplished by the thermal energy supplied by a focused and computer controlled laser beam. For the production of functional metallic prototypes, parts or tools, a high part density is desired and this can be obtained from SLM without any post-processing steps. The other competitive advantages of SLM include geometrical freedom, mass customization, material flexibility and short time service. In the literature, SLM technology is very similar to selective laser sintering (SLS). However, SLS obviously fabricates the parts from mixture of powder and binding material whereas, SLM builds up the parts directly from powder. A distinction of these two methods is summarized in Table 1.1.

Table 1.1 Comparison the most important differences between SLS and SLM

Process	Selective laser sintering (SLS)	Selective laser melting (SLM)
Binding mechanism	- Full melting - Liquid phase sintering full melting - Partial melting	Full melting
Materials (cf. bind, mech.)	- Polymers - Special powders (binder) - special metal powders	Standard metals or metal alloys
Thermal source	Mostly CO_2 laser	Nd:YAG / Yb:YAG laser
Energy input	Low	High
Support	-	Base plate

Process

Figure 1.3 shows the configuration of a typical SLM system, the part is fabricated in a build chamber and a feed powder chamber stores the powder. After lowering the build chamber and raising the feed powder chamber, a scraper in a power coating system deposits the first layer of the powder on a base plate in the build chamber. The first layer of the part, as calculated as the first horizontal cross-section of the CAD model, is then scanned with a laser. The laser beam is focused by the f-θ lens and us deflected by two galvano mirrors which are controlled the movement of the beam on the powder bed. The powders particles heat up depended on absorption of the laser radiation and bind to each other and to the based plate underneath. The process is carried out in a protective nitrogen gas to avoid oxidation of the material. The process of powder deposition and laser scanning is repeated layer-by-layer for every cross-section until the 3D part will be created. Finally, the parts are removed from the SLM machine.

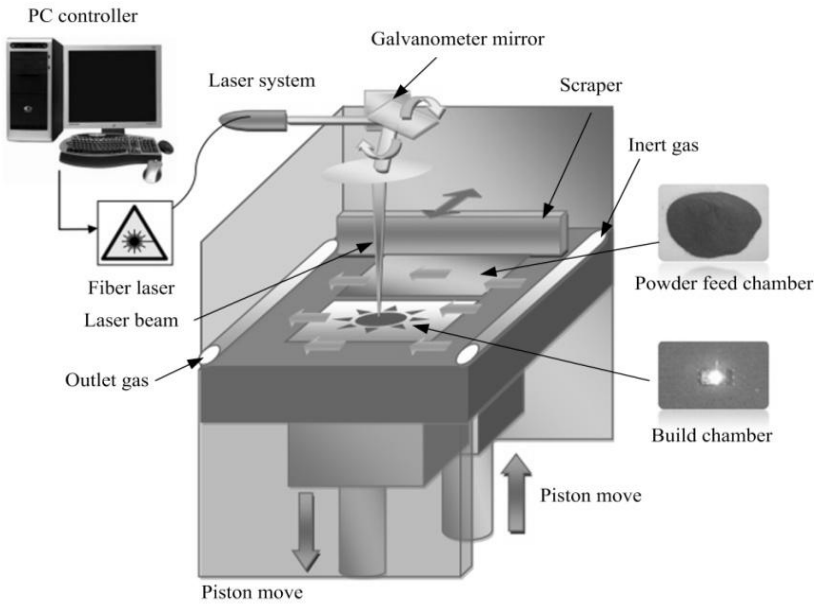

Figure 1.3: Basic principle of selective laser melting.

1.2 Statement of problem

High density with high geometric freedom of metal parts can be fabricated using SLM method and the metal parts has mechanical properties superior to those conventional process (Kruth et al., 2005; Kumar, 2008). It can say that SLM is an emerging technology with a high potential. The interest from both research and commercial is on demand. To date, there are different SLM machine available and offer to fabricate a complex prototype. However, the production process is still limited. Many research studies Kruth et al., 2004; Gu and Shen, 2009; Li et al., 2010 have shown that mechanical properties of full dense parts fabricated using laser were lower than standard level. The formation of SLM parts is varied depending on 50 parameters or higher. The failure of SLM process could be present as a balling, vaporization, oxidation, wetting between layers, residual stress and deformation.

Optimal process parameters have been studied by many researches in order to improve the quality of final part, minimize manufacturing cost and shorten manufacturing time. A classical design of experiment (DOE) is commonly used as a methodology to optimize RP process, electron beam machining, laser drilling and laser welding (Kruth et al., 2004; Dingal et al., 2004; Mumtaz, Erasenthiran, and Hopkinson, 2008).

From these overviews of authors that used a formal methodology/DOE in production, it is cleared that this methodology was not frequent but the fact that most of the published work had a substantial amount of experimental work. Therefore, this study used DOE methodology which was called that factorial analysis to optimize processing parameters including laser power, scan speed, scan spacing and scan strategy. Due to these parameters can be controlled easily and had direct influence to the final parts (Van Elsen, 2007; Mumtaz, Erasenthiran, and Hopkinson, 2008; Zhang et al., 2009; Yadroitsev et al., 2007)

1.3 Rationale

Although SLM provides many advantages and has widely used in many engineering fields but the physical phenomena of SLM process are rather complex and depend on many parameters in processing. In order to overcome this problem, process parameters of SLM

were optimized based on DOE methodology in this study. The study of this experiment was carried out based on 2 hypotheses (i) if the final quality of parts is influent by laser power, scan speed, scan spacing and scan strategy and also (ii) to compare mechanical properties the fabricated parts obtained from optimal SLM process with ASTM (A240/A240M-04); a standard properties of 316L stainless steel bars and shapes (hot-finished).

1.4 Objectives

The purposes of this study are:

- To optimize process parameters including laser power, scan speed, scan spacing and scan strategy for fabrication of fully dense stainless steel 316L parts during SLM process.
- To investigate the rapid prototyping performance in fabrication of fully dense stainless steel 316L parts as well as to compare properties of parts after process by SLM technology with parts of standard properties ASTM (A240/A240M-04).

1.6 Scope and limitation of study

- All experiments in this study were carried out using an in-house SLM machine, equipped with a high laser output of 300 W Ytterbium fiber laser (National Metal and Materials Technology Center, Thailand). The machine can build up a layer as minimum as 100 μm.
- The parts were built layer by layer on the stainless steel 316L powder under a nitrogen atmosphere.
- The study was divided into two major steps. First part, process parameters including laser power, the exposure time that resides at each point (scan speed), the distance between the laser hatches (scan spacing), scan strategy were optimized in order to fabricate the parts using stainless steel 316L powder. The tests were performed based on 2^k factorial design. The responses of the process were measured base on density, hardness and build rate (scanning rate) of the parts.

- Second parts, the experimental data obtained from the first part were used to fabricate parts. Tensile test, study of microstructure and elemental on the surface of the fabricated parts were carried out with electron probe micro-analyzer.

1.7 Theory and review related literatures

1.7.1 Selective laser melting (SLM)

SLM is a solid freeform fabrication process whereby a 3D part is built layer-by-layer using high power laser to melt powder particles completely. Consequently, the binding mechanism of powder base is called Full Melting, as will be discussed in detail in section 1.7.2. In theory, all metals or metal alloys can be used in SLM processes but the range of commercially metals powder for SLM remains limit due to different physical properties of the materials during processing. Nowadays, typical standard materials of SLM technologies are widely used such as tool steel (H13), stainless steel (316L), pure titanium, titanium alloy (Ti-6Al-4V), cobalt-chromium alloys (ASTM75), and two aluminum alloys powders (Al-12Si-Mg and Al-10Si-Mg) (Wohlers, 2009). Other materials were researched such as Inox 904L (Yadroitsev, Bertrand, and Smurov, 2007), Wasploy (Mumtaz, Erasenthiran, and Hopkinson, 2008), Inconel (Kamran and Neil, 2009), Stainless steel 316L combined with Hydroxyapatite (Hao et al., 2009), Gold (Khan and Dickens, 2010) and so on. In addition, Kruth et al., 2007 concluded the major benefits and drawbacks of SLM as follows:

Benefits

- Materials need not to use binder thus the process can produce “single material” parts rather than producing a composite green part which may not be desired.
- SLM can eliminate time of consuming and costly furnace post-processes.
- SLM can produce full dense parts (even over 99.9%) in a direct way by without post infiltration, sintering or HIPing.

Drawbacks

- SLM still have a limit for building of the composite materials.
- The laser powder processing needs high laser power, good beam quality which is very expensive laser and low scan velocities.
- The quality of specimen rather than low quality of facing surfaces, higher upper surface roughness, risk of internal pores and higher residual stresses.

1.7.2 Full melting

SLM is process which uses a high energy density to melt the powders. Full melting is the mechanism most usually related with powder bed fusion processing of metal alloys and polymers. Thermal energy of a laser type is very effective at creating well-bonded, high-density structure from metal alloys and polymers. Thus, the fabricated parts exhibit a density very close to the hypothetical. However, the large differences occur in the case of processing such as laser absorption, surface tension, viscosity of the liquid metal and so on, which depend on type of materials. Each new material, a process need to be determined experimentally in order to avoid scan track instabilities (called “balling”) and part porosity.

1.7.3 Processing parameters

SLM is complex thermo-physical processes which have many physical phenomena occurred in a very short time (millisecond) and depend on more than 50 parameters that possibly influence the process (Van Elsen, 2007). In this research is divided SLM parameters into four main groups including environmental, laser, material and scanning parameters and this section will give a brief overview of these four groups as follows:

(1) Environmental parameters

The first parameter should be controlled in SLM is gas system within the process chamber to protective non-inert particles. Especially, oxygen gas can react with the molten metal and have influence with the final properties of the component. Hauser et al., 1999 described that the contamination of oxygen in process caused reduction of surface energy and increased instability of melt pool. In addition, the some typical elements of process have

susceptibility with oxidation are Si, Al and Ti. Consequently, inert gas (Ar, He) or non-active gas (H_2, N_2) is used to protect oxidation. However, H_2 and N_2 gas can be dissolved into solution cause reducing the corrosion resistance and embrittlement (Rombouts, 2006) Therefore, types of inert/non-active gas is emphasized. For stainless steel, N_2 is used.

(2) Laser parameters

Many lasers such as CO_2 laser, Nd:YAG laser, diode laser, disk laser and fiber laser is developed for selective laser melting. Nowadays, the fiber laser is receiving attention due to its advantages of high power, high beam quality, simplicity, high electrical to optical efficiency, reliability, excellent thermal properties, robustness and low running cost (Joo et al., 2009). In the SLM process powder is melted by heat up to the powder bed of a laser system which depends on parameters as follows:

- **Wavelength** of the laser can determine the absorptivity and also influence the resolution.
- **Laser mode** has two modes including continuous wave mode and pulsed mode. For continuous wave mode no cracks is formed in parts because the interaction between laser beam and powder material happen more smoothly and smaller. However, thermal stress is formed due to the lower thermal gradients and not fully molten state of the material. Contrast, pulse mode lead to more dense parts with more homogeneous microstructure. This mode is the really vehement interactions between laser beam and powder material. It is very short time and high power pulses which lead to high thermal gradients and high cooling rates are cause high thermal stresses and rather brittle material (Ben, 2008).
- **The focus diameter or spot size** (d_x) is taken as the distance perpendicular to the speed of moving laser source which is defined as equation (1.1):

$$d_x = (\lambda \cdot f \cdot M^2 \cdot k)/d \tag{1.1}$$

with λ the wavelength, M^2 the beam quality (1.05), f the focal length (typically 500 mm), k the correction factor (ideally 1.79), and d the beam diameter prior to focusing (19 mm).

- **Laser power intensity** is a first importance process parameter (I) due to it determines how much heat add on a specific place is defined as equation (1.2) :

$$I = \frac{P}{\pi r^2} \tag{1.2}$$

with P the power laser and r the radians of laser beam (Rombouts, 2006).

(3) Material parameters

The SLM technique can use with wide materials polymer, metal, ceramic and composite but the ranges of commercially use powders for laser metal processing is limited today. Consequently, the SLM processing will be easier or more difficult depends on the chemical composition and physical properties of the chosen material as follows:

- **Powder particle morphology** should be spherical because the particle shape influence with the flow ability of the powder which have importance for the deposition of a layer. In addition, the average particle size and particle size distribution determine the powder density and properties of the powder bed (Simchi, 2004 and Ruidi et al., 2010).
- **Density** of the powder materials can determine the maximum final density of the component and have an important influence on the heat balance. The density has influence on the expelling of particles from the melt pool. If particles has a low density and low mass, it are expelled more easily (Simchi, 2004; Van Elsen, 2007).
- **The absorption coefficient** is the effect about the reflectivity for opaque materials.

$$\text{Absorptivity} = 1 - \text{Reflectivity} \tag{1.3}$$

Thus, the absorptivity of metals is very low in the waveband from visible to the direct current that is very long wavelengths as shows in Figure 1.4. The ratio of the absorpsion depends on type of powder beds and completely dense materials. For this thesis studies 316Lstainless steel materials. The hemispherical reflectivity of pure iron R = 0.7 is accepted for 316L stainless steel at the laser wavelength of 1.06 μm by Gusarov et al. 2007.

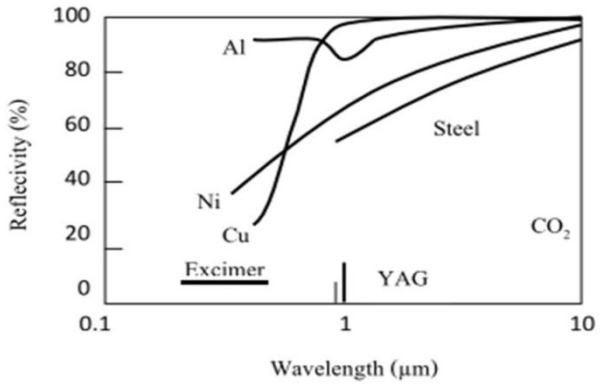

Figure 1.4: Reflectivity of metals as a function of wavelength (Steen, 2003).

- **The melt enthalpy** is the amount of energy need to melt the powder completely and it can determine the heat balance equation follows:

$$\delta h = \rho C_p (T_m - T_\infty) + \rho L_T \tag{1.4}$$

with T_m the melting temperature (K), T_∞ the ambient temperature (K), ρ the density (kg m^{-3}), L_f the latent heat of fusion, C_p the specific heat capacity ($m^2 s^{-2} K^1$).

- **The thermal conductivity** of the bulk material is important for the conductivity of the powder material which has influence on the heat balance.
- **Latent heat of fusion** during melting, a material absorbed an amount of energy in order to realize the change of phase. This energy is the latent heat of fusion. The same amount of energy is fed during solidification. This factor has influence on the heat balance and the latent heat of fusion results elongation (Van Elsen, 2007).

(4) Scanning parameters

The fabrication of the parts is done by scanning a pattern of lines on the surface, laser by layer. Therefore, the setting of scanning parameters has strong influence the heat balance, the building speed and the accuracy. The scanning parameters are concluded as follows:

- **Scan strategy** is used to fill a cross-section by scan track. The cross-section subdivided in sectors and scan pattern as shows in Figure 1.5 (a) Zig-Zag, (b) Parallels, (c) Spiral, (d) Hatching (e) Chessboard.

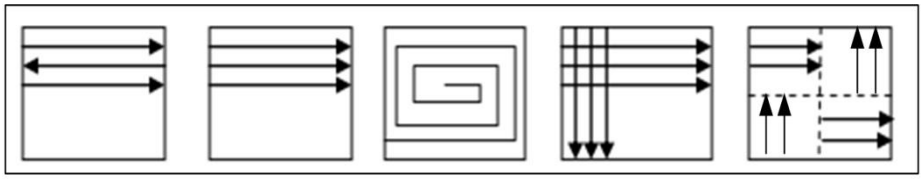

Figure 1.5: Scan strategies existing in the software AutoFab (a) Zig-Zag, (b) Parallels, (c) Spiral, (d) Hatching (e) Chessboard of a layer in sectors.

These scan strategies have an influence the temperature distribution in the part. Matsumoto et al., 2002; Kruth et al., 2004; Zhang et al., 2009 explained that when the part area was divided in small sector and scan successive can reduce deformation (Warpage, Cracking) due to the influence of heat temperature. Childs, Hauser, and Badrossamay 2004 suggested that laser scan lengths should be less than 10 mm. Especially, cases of machine without preheat system.

- **Scan spacing or Overlapping (Ss)** is distance between two successive scan tracks, which its value is normally lower than the laser beam diameter as shows in Figure 1.6. In addition, the dimensionless parameter can be related to the percentage of overlap $\%S_s$, defined as:

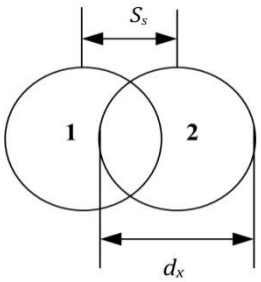

$$\%S_s = 1 - \frac{Ss}{d_x} \quad (1.5)$$

Figure 1.6: Percentage of overlap between two successive scan tracks by Ss the scan spacing and d_x the beam diameter.

By an overlap of 0 means that scan tracks do not touch. An overlap of 1 means scanning the same track twice and from the experiments, it is observed that a value of the scan spacing fulfill is defined as follows:

$$\frac{Ss}{d_x} < 0.05 \quad (1.6)$$

The processing conversion from irregular surface to a smooth surface occurs from decreasing scan spacing and obtained a homogeneously density part (Van Elsen, 2007).

- **Scan speed (V)** of scanning have a major influence on the heat balance and have an influence in a lower and higher building time.
- **Layer thickness (L_t)** of powder deposited layer on based plate and must be melted by a single scan track. Figure 1.7 shows that a slight layer thickness is not only useful for improving the final surface but also tend to result in a better accuracy of the desired shape. Normally, all the RP technique have comparable performances in accuracy (0.05 - 0.2 mm on 100 mm) and surface finish (R_a = 5 - 20 µm) (Rombouts, 2006).

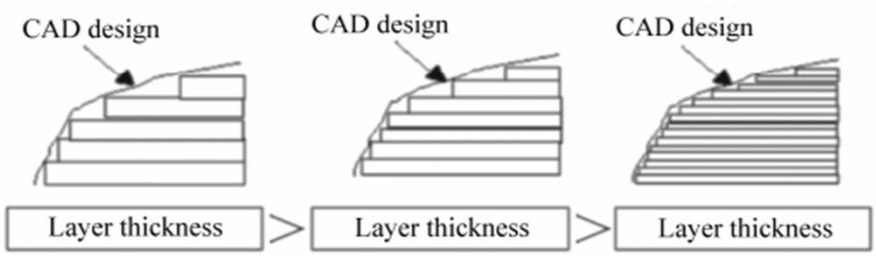

Figure 1.7: Effect of layer thickness on stair case effect.

The commercially accepted quality parts, when layer thickness is average less than 100 µm and even as small as 30 µm (Childs, Hauser, and Badrossamay, 2004). But it will decrease the speed of the process

- **Energy density (E_{dens})** is the laser beam to a volumetric unit of powder material as equation follows:

$$E_{dens} = \frac{P}{VSsL_t} \tag{1.7}$$

Four parameters of this equation have a large influence on the part density, when applied energy increase with increasing laser power and decrease with increasing velocity and scan spacing (Ben and Jean-Pierre, 2007).

1.7.4 Fluid behavior

The fluid behaviors of the molten pool during SLM have influence on the morphology of the surface and density of the part. In the idea case, the liquid pool create during SLM should spread well over the underlying solid and remain continuous along the direction of the laser motion but the behavior during SLM is often far from idea. Therefore, it is a need to understand the phenomena are responsible for this behavior such as surface tension and wetting.

Surface tension (γ) and Wetting: the liquid droplets tend to be spherical because the sphere has the smallest surface area for its volume. This elastic force is the relative attraction among molecules in a liquid. The elastic force decrease when temperature is

increased. For the surface tension of liquid and solid metals are discussed by Eustathopoulos, Nicholas, and Drevet, 1999. They had the reliable values of γ_{LV} of pure metals for most commonly used metals. Many authors described that the balling occurred from the molten material did not wet the substrate. Then the surface tension, liquid tend to spherical and obstructing a smooth layer deposition of the parts. This metastable equilibrium was shown in Figure 1.8 and Young' s equation (1.8):

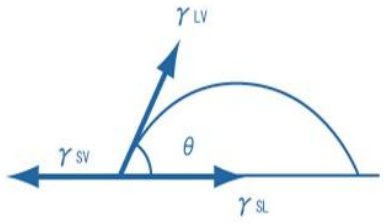

$$\gamma_{SL} + \gamma_{LV} cos\theta = \gamma_{SV} \qquad (1.8)$$

Figure 1.8: Wetting of a liquid on a substrate as described by Young's equation (Rombouts, 2006).

with the surface tensions γ_{SV}(solid-vapour), γ_{LV} (liquid-vapour) and γ_{SL}(solid-liquid). If a contact angle of less than 90º identifies a wetting liquid, while a greater value recognize a non-wetting liquid but if the contact angle is zero, the liquid is considered to be perfectly wetting. Therefore, the value of θ obeys the classical that Young's equation (Kruth et al. 2004).

Gu et al., 2009 explained that the liquid was much easy to flow, spread, and wet the un-melted solid particle cores, favoring a sufficient rearrangement of particles under the action of capillary forces exerted on them by the wetting liquid. The spreading and flattening of the molten materials on the underlying substrate was, thus, realized, leading to a significant increased in the diameter of the molten track. According to the perturbation theory, the capillary instability of the melt decreased due to a larger cylindrical melt formed under laser irradiation, leading to the formation of coherently bonded track free of any balling phenomenon after melting. Yadroitsev et al., 2010 discussed that the capillary instability of a liquid indicates cylinder was stable against

axial harmonic disturbances of its radius with wavelengths less than the circumference of the cylinder. Therefore, the necessary and sufficient condition of stability as follows:

$$\frac{\pi D}{\mathrm{L}} > 1 \tag{1.9}$$

with D the diameter and L the wavelength. If a fluid cylinder free in space is unstable, when the ratio of length πD to radius L exceed 1 as well as Khan and Dickens, 2010 found that at higher scan speeds observed the balling effect. Due to the length of the melt pool increases and a reduction in the melt pool width thus increasing the $\pi D/L$ ratio over 1 and destabilizing the melt pool. Whereas, at low scan speeds, the molten material have much greater time to be in the molten state compared to higher scan speeds. At low scan speeds appeared balling due to the high energy input and greater time available for the molten metal to split into smaller droplets before resolidification.

In addition, the fluid motion occurs in melt pools with non-uniform temperature during SLM. The thermocapillary flow (convection flow) is the fluid motion in melt pools due to instability of the temperature and concentration of some element such as (S, O, Se, Te) in the alloy which have an influence to the surface tension of a liquid metal. The direction of the thermocapillary flow is determined by the concentration of S or O in the alloy and occur from a region of low surface tension to a region of high surface tension as shows in Figure 1.9 (a) at S or O concentration > 50 ppm, the surface tension decreases with increasing temperature (negative surface tension gradient) whereas, at S or O concentration > 60 ppm the surface tension increases with increasing temperature (positive surface tension gradient) as shows in Figure 1.9 (b)**.** Therefore, these convective flows cause a significantly different temperature distribution.

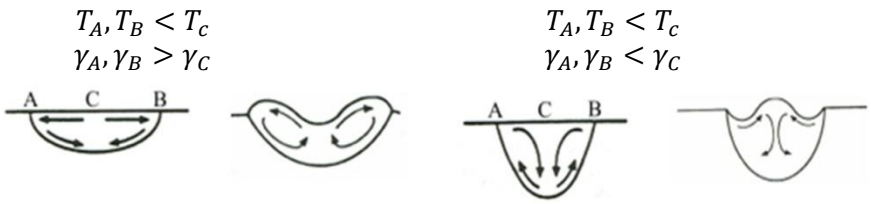

(a) $\frac{d\gamma_{LV}}{dT} < 0$ (b) $\frac{d\gamma_{LV}}{dT} > 0$

Figure 1.9 Schematic of Marangoni flow due to a temperature gradient in a liquid pool for a material with (a) negative $\frac{d\gamma_{LV}}{dT}$ (outward surface flows with downward flow at periphery of melt pool) and (b) positive surface tension gradient $\frac{d\gamma_{LV}}{dT}$ (inward surface flows with downward flow in center) (Mills et al., 1998).

1.7.5 Thermal conductivity

During SLM process the thermal is occurred by the moving heat source, which is caused of physical state changes, metallurgical phase transformations, thermal stresses and finally fluid motions. These phenomena are suggested using the knowledge about welding or laser processing. The thermal conductivity (λ) is a parameter that has a large impact on the heat transfer during SLM and it depends on the state of the material which can be powder, liquid or solid during process. Normally, the ranges of thermal conductivity for metals from about 8 W/(mK) to 400 W/(mK) (Van Elsen, 2006).

However, the conductivity of metals generally decreases due to increasing temperature. (Gusarov et al., 2007) described that the thermal conductivity of 316L stainless steel considerably increase with temperature above the room temperature. The temperature range about the melting point and above is the most important. This experiment accepts a constant value of thermal conductivity is 20 W/(m K), which it obtains from extrapolation to the melting point. In addition, some authors use a constant value of thermal conductivity for analysis is 16.2 W/(mK). The effective thermal conductivity of loose metallic powders is independent of material but depend on the size and morphology of the particles and the void fraction. For 10–50 mm powders the effective thermal conductivity is typically from 0.1 to 0.2 W/(m K) in air at room temperature.

1.7.6 Thermal deformation

The temperature gradient mechanism (TGM) is mechanism in SLM which is acts on previously solidified layers lying underneath the processed powder layer. Rombouts, 2006 explained that the rapid melting of the higher surface by the laser beam and the rather low heat conduction, a steep temperature gradient occurred. Therefore, the material strength reduced due to increasing of temperature. Expansion of the heated top layer (ε_{th}) was changed elastic to plastic compressive strains as shows in Figure 1.10 on account of the adjacent material restrain a free expansion. When the material yields stress, the top layer will be plastically compressed (ε_{pl}, σ_{comp}). If it did not have mechanical constraints, a counter bending away from the laser beam would be observed. During cooling and shrinkage, the plastically compressed upper layers became shorter than the bottom layers and a bending angle towards the laser beam developed. These effects were cause of distortion and part failure by cracking. The temperature gradient had an influence with the shrinkage of the molten layer during cooling added additional tensile stresses on top of the layers underneath. Only the temperature changed below the melting point results in additional stresses in the newly deposited layer. These stresses also tended to bend the part towards the laser.

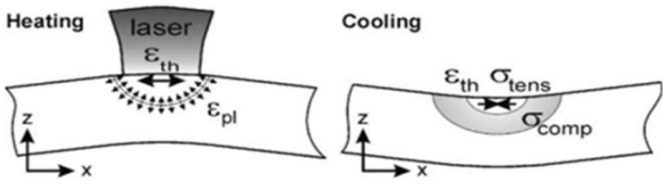

Figure 1.10: Temperature gradient mechanism (Kruth et al., 2004).

1.7.7 Different process temperatures

Kruth et al., 2004 described that the building of parts should be scanned was small area. Because the adjacent tracks are scanned rapidly one after the other, leaving little cool down time in between thus resulting in high temperatures. On the other hand, if larger areas the laser beam travel distance are much longer. And successively scanned tracks have more time to cool down leading to a lower temperature of the scanned area. Therefore, worse wetting conditions are presented leading to a lower density of the material. Meanwhile,

Osakada and Shiomi, 2006 studied about thermal distortion by finite element and found that the model tended to be deformed and cracked due to thermal stress appear at the left-side end of the layer and higher when length of scanning track increases after solidified part is cool rapidly. Consequently, they suggested that should divide into small segments of large area before scanning. The different process temperatures occur from the difference in heat conductivity between the loose powder bed and the solidified material. During laser is melting powder bed, the material density increases (e.g. from 40 to 95% of the true density). When scanning small area surround by loose powder, it is compared with large zones which is less heat sink because the isolation of the adjacent powder. Therefore, the locations have higher temperature which can lead to better wetting conditions and higher material densities.

1.7.8 Gas entrapment

Gas bubbles occur during solidification, it can become entrapped in the material if their growth rate is about the same or lower than the solidification speed. The causes for bubble generation are considered as follows:

- decrease in the solubility of the dissolved elements in the molten pool during cooling and solidification
- chemical reaction
- evaporation of elements with a high vapour pressure
- trapped gas

In welding, the first cause of bubble formation is often observed for elements such as nitrogen, oxygen or hydrogen when dissolved, for example in iron and aluminum. For SLM, gas can also form during processes because the reaction of elements in the material with the atmosphere. For instance, in carbon steels carbon can react with oxygen to form gaseous products as CO or CO_2. In addition, convection in the molten pool, such as convection flow can decrease or increase the amount of entrapped pores depending on its direction (Rombouts, 2006).

1.7.9 Microstructure characteristic of rapidly cooled and solidified materials

Due to SLM parts is built with high cooling rates, the short interaction time and high thermal gradients which can observe some micro-structural characteristics of materials. Rombouts, 2006 described that the growth morphology of the interface during solidification can be planar, dendrite or cellular depending on the thermal and constitutional conditions in the immediate vicinity of the interface.

Many authors studied microstructure of stainless steel for instance; Kruth et al., 2010 found that the cross-section of the AISI 316L part revealed a fine cellular-dendrite structure (Kumar, 2008) of stainless steel, which was supplied by Concept Laser GmbH and EOS stainless steel by EOS GmbH. It is found that microstructure of final parts of both material appear dendrites structure by dendrite was formed due to the creation of high thermal gradients during SLM and the dendrite had different direction of their growth corresponding to different direction of cooling of the melt pool. If it made the highest-angle grain boundaries with neighbors it can result of potential cracks or fractures. In addition, stainless steel part of EOS was annealed samples. Microstructure appeared the grain shapes unlike the grain shapes found earlier. But it looks like approaching circles because the stress-relieving heat treatment which helped diffusion to take place and reshaped the existing grain.

1.8 Design of experiments (DOE)

In the early days of experimental design, only main effects were considered. Later, the interactions between two factors were also studied. Nowadays, the interactions between three factors are taken into account as well. Frequently used are the 2^k ($2 \times 2 \times \ldots. \times 2$) Factorial designs are used to determine the effects of k factors, each of which have two alternatives or levels. Due to, it is easier to analyze than full factorial designs and can provide the smallest number of runs which k factors can be studied in a complete factorial design because there are only two levels for each factor. The statistical model for a 2^k design would include k effects, $\binom{k}{2}$ two-factor interaction, $\binom{k}{3}$ three-factor interactions,…., and one k-factor interaction. That is, for a 2^k design the complete model would contain $2^k - 1$ effects. For example, 2^3 design is (1), a, b, ab,

c, ac, bc and abc. There are levels of factor A, b levels of factor B and c levels of factor C. The general approach to the statistical analysis of the 2^k design as follows:

Step 1: This step is estimation of factor effects and examines their signs and magnitudes. This gave the experimenter preliminary information regarding which factors and interactions may be important, and in which directions these factors should be adjusted to improve the response.

Step 2: The forming the initial model for the experiment, it is usually chosen the full model, than is all main effects and interactions, provided that at least one of the design points has been replicated. For example, 2^4 factorial designs, which have the type of 2^k design in 4 factors (A, B, C and D) and can represent by the linear statistical mode as equation (10):

$$y_{ijklm} = \mu + \tau_i + \beta_j + \gamma_k + \delta_l + (\tau\beta)_{ij} + (\tau\gamma)_{ik} + (\beta\gamma)_{jk} + (\tau\delta)_{il} + (\beta\gamma)_{jk} + (\beta\delta)_{jl} + (\tau\beta\gamma)_{ijk} + (\beta\gamma\delta)_{jkl} + (\tau\beta\gamma\delta)_{ijkl} + \epsilon_{ijklm} \quad (1.10)$$

$$i = 1,2 \rightarrow j = 1,2 \rightarrow k = 1,2 \rightarrow l = 1,2 \rightarrow m = 1,2, \ldots, n$$

Where is μ is the overall mean effect, τ_i is the effect of the *i*th level of factor A, β_j is the effect of the *j*th level of factor B, γ_k is the effect of the *k*th level of factor C, δ_l is the effect of the *l*th level of factor D, $(\tau\beta)_{ij}$ is the effect of the interaction between A and B, $(\tau\gamma)_{ik}$ the effect of the interaction between A and C, $(\beta\gamma)_{jk}$ is the effect of the interaction between B and C, $(\tau\delta)_{il}$ is the effect of the interaction between A and D, $(\beta\gamma)_{jk}$ is the effect of the interaction between B and C, $(\beta\delta)_{jl}$ is the effect of the interaction between B and D, $(\tau\beta\gamma)_{ijk}$ is the effect of the interaction between A,B and C, $(\beta\gamma\delta)_{jkl}$ is the effect of the interaction between B, C and D, $(\tau\beta\gamma\delta)_{ijkl}$ is the effect of the interaction between A,B, C and D is the effect of the interaction between A,B and C, and ϵ_{ijklm} is a NID $(0, \sigma^2)$ random error component.

Step 3: The Analysis of Variance or ANOVA, also developed by Sir Ronald Fisher in the 1930s. It is used to test the differences in averages between different treatments. The Fisher test or F-testis used to estimate the significance of the variance of the treatment means, compared to the residual variance. For example 2^3 factorial design and eight treatment combinations can be displayed graphically as a cube, as shows in Figure 1.11(a). The treatment combinations is written

in standard or as (1), a, b, c, ab, ac, bc, and abc. There are the + and – notation are widely used for the runs in the 2^k design as shows in Figure 1.11(b). There is seven degrees of freedom between the eight treatment combinations in the 2^3 design. Three degrees of freedom are associated with the main effects of A, B and C. Four degrees of freedom are associated with interactions; one each with AB, AC and BC and one with ABC.

$$B = \bar{y}_{B^+} - \bar{y}_{B^-} = \frac{1}{4n}[a - (1) - ab - b + ac + c + abc - bc] \tag{1.11}$$

$$C = \bar{y}_{C^+} - \bar{y}_{C^-} = \frac{1}{4n}[a - (1) + ab - b + ac - c + abc + bc] \tag{1.12}$$

For interaction, A measure of the AB interaction is difference between the averages A effects at the two levels of B. Thus convention, one-half of this difference is called the AB interaction. Since, the calculating of the two-factor interactions is:

$$AB = \frac{1}{4n}[abc - bc + ab - b - ac + c - a + (1)] \tag{1.13}$$

$$AC = \frac{1}{4n}[abc - bc - ab + b - ac - c - a + (1)] \tag{1.14}$$

$$CB = \frac{1}{4n}[abc + bc - ab + b - ac + c - a + (1)] \tag{1.15}$$

Consider estimating the main effect:

$$A = \bar{y}_{A^+} - \bar{y}_{A^-} = \frac{1}{4n}[a - (1) + ab - b + ac - c + abc - bc] \tag{1.16}$$

The ABC interaction is defined as the average difference between the AB interactions for the two different levels of C Thus:

$$ABC = \frac{1}{4n}\{[abc - bc] - [ac - c] - [ab - b] + [a - (1)]\} \tag{1.17}$$

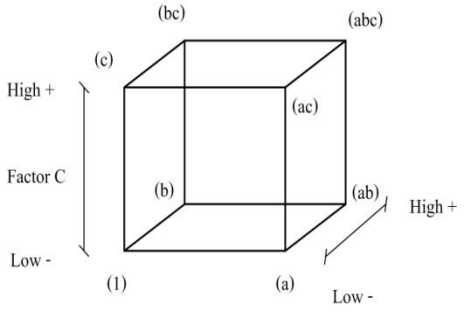

(a) Graphic 2^3 factorial

Treatment combination	Factor						
	A	**B**	**C**	**AB**	**AC**	**BC**	**ABC**
(1)	-	-	-	+	+	+	-
a	+	-	-	-	-	-	+
b	-	+	-	-	+	+	+
c	+	+	-	+	-	-	-
ab	-	-	+	-	-	-	-
ac	+	-	+	-	+	-	-
bc	-	+	+	-	-	+	-
abc	+	+	+	+	+	+	+

(b) The design matrix

Figure 1.11 (a) Geometric views and (b) Algebraic signs for calculating effects in the 2^3 design.

Table 1.2 Data arrangement for a 2^3 factorial design

Factor A	Factor B			
	b_1		b_2	
	Factor C		Factor C	
	c_1	c_2	c_1	c_2
a_1	$y_{1111}, y_{1112}, y_{1113}, y_{111n}$	$y_{1121}, y_{1122}, y_{1113}, y_{111n}$		$y_{1221}, y_{1222}, y_{1223}, y_{122n}$
a_2	$y_{2111}, y_{2112}, y_{2113}, y_{211n}$	$y_{2121}, y_{2122}, y_{2123}, y_{212n}$		$y_{2221}, y_{2222}, y_{2223}, y_{222n}$
a_1				
a_2	y_{a_2111},……., y_{a_211n}	y_{a_2121},……., y_{a_212n}		y_{a_2221},……., $y_{a_2b_2c_2n}$

In equations 1.18 through 1.20, the quantities in brackets are called contrasts. Therefore, table of plus and minus signs can be developed form the contrast. Sums of squares in Table 1.2 are obtained. Each effect has a corresponding single-degree-of freedom contrast. In the 2^3 design with n replicates, the sum of squares for A, B, C, AB, AC, BC and ABC effect is:

$$SS = \frac{(Constrast)^2}{8n} \tag{1.18}$$

The total sum of squares is found in the usual way, that is:

$$SS_T = \sum_{i=1}^{a}\sum_{j=1}^{b}\sum_{k=1}^{c}\sum_{m=1}^{n} y_{ijk}^2 - \frac{y_{....}^2}{abcn} \tag{1.19}$$

The error sum of squares may be found by subtracting the sum of squares for each main effect and interaction from the total sum of squares by:

$$SS_E = SS_T - SS_A - SS_B - SS_{AB} \tag{1.20}$$

Table 1.3: The analysis of variance table for the four factor fixed effects mode (Montgomery, 1991)

Factors	**SS**	**DF**	**Mean Square**	**Expected mean squares**	**F**
A	SS_A	a-1	$MS_A = \frac{SS_A}{a-1}$	$\sigma^2 + \frac{bcdn\sum \tau_i^2}{a-1}$	$\frac{MS_A}{MS_E}$
B	SS_B	b-1	$MS_B = \frac{SS_B}{b-1}$	$\sigma^2 + \frac{acdn\sum \beta_j^2}{b-1}$	$\frac{MS_B}{MS_E}$
C	SS_C	c-1	$MS_C = \frac{SS_C}{c-1}$	$\sigma^2 + \frac{abdn\sum \gamma_k^2}{c-1}$	$\frac{MS_C}{MS_E}$
D	SS_D	d-1	$MS_D = \frac{SS_D}{d-1}$	$\sigma^2 + \frac{abcn\sum \delta_l^2}{d-1}$	$\frac{MS_D}{MS_E}$
AB	SS_A	(a-1)(b-1)	$MS_{AB} = \frac{SS_{AB}}{(a-1)(b-1)}$	$\sigma^2 + \frac{cdn\sum\sum(\tau\beta)_{ij}^2}{(a-1)(b-1)}$	$\frac{MS_{AB}}{MS_E}$
AC	SS_{AC}	(a-1)(c-1)	$MS_{AC} = \frac{SS_{AC}}{(a-1)(c-1)}$	$\sigma^2 + \frac{bdn\sum\sum(\tau\gamma)_{ik}^2}{(a-1)(c-1)}$	$\frac{MS_{AC}}{MS_E}$
BC	SS_{BC}	(b-1)(c-1)	$MS_{BC} = \frac{SS_{BC}}{(b-1)(-1)}$	$\sigma^2 + \frac{adn\sum\sum(\beta\gamma)_{jk}^2}{(b-1)(c-1)}$	$\frac{MS_{BC}}{MS_E}$
ABC	SS_{ABC}	(a-1)(b-1) (c-1)	$MS_{ABC} = \frac{SS_{ABC}}{(a-1)(b-1)(c-1)}$	$\sigma^2 + \frac{dn\sum\sum\sum(\tau\beta\gamma)_{ijk}^2}{(a-1)(b-1)(c-1)}$	$\frac{MS_{ABC}}{MS_E}$
Error	SS_E	abc(n-1)	MS_E	σ^2	
Total	SS_T	abcn-1			

Step 4: Refining the model, usually consist of removing any non-significant variable from the full model**.**

Step 5: It is the usual residual analysis to check for model adequacy and to check assumptions. The residuals from a three-factor factorial are:

$$e_{ijkl} = y_{ijkl} - \bar{y}_{ijk} \qquad \begin{cases} i = 1,2,\ldots..,a \\ j = 1,2,\ldots..,b \\ k = 1,2,\ldots..,c \\ l = 1.2.\ldots...n \end{cases} \tag{1.21}$$

That is, the residuals $\left(e_{ijkl}\right)$ are just the difference between the observations and the corresponding averages. Table 1.2 y_{ijkl} be observed response when factor A is at the *i* th level, factor B is at the *j* th level, factor C is at the *k* th level for the *l* th replicate. Define $\bar{y}_{i\ldots}$, $\bar{y}_{j\ldots}$, $\bar{y}_{k\ldots}$, $\bar{y}_{l\ldots}$, $\bar{y}_{ij\ldots}$,……, $\bar{y}_{ijk\ldots}$ and $y_{ijk\ldots}$ as the corresponding row, column, cell and grand averages. To construct a normal probability plot, arrange the residuals in increasing order and plot the *K* th of these order residuals versus the cumulative probability point $P_K = (K - 1/2)/N$ on normal probability. If the underlying error distribution was normal, this plot will resemble a straight line. However, if the model is correct, the residual should be particular structureless. The residual vs. order and the residual vs. the fitted valued $(\bar{y}_{ijk})$ plot should not reveal any obvious pattern. Moreover, the histogram plot between the residual vs. frequency should be bell shape.

Step 6: Usually consists of graphical analysis either main effect or interaction plots, optimize analysis and regression model:

$$y = \beta_0 + \beta_A x_A + \beta_B x_B + \varepsilon \tag{1.22}$$

Where x_A and x_B are coded variables that represent the two factors, i.e. x_A (or x_B) only take values on –1 and 1, β's are regression coefficients and ε is error of response.

CHAPTER 2

Research Methodology

2.1 Experimental Methodology

Selective laser melting experiments using 316L stainless steel powder was performed. Each layer was built at a constant thickness of 100 μm for single line scanning and multiple layers scanning experiments shown in Figure 2.1

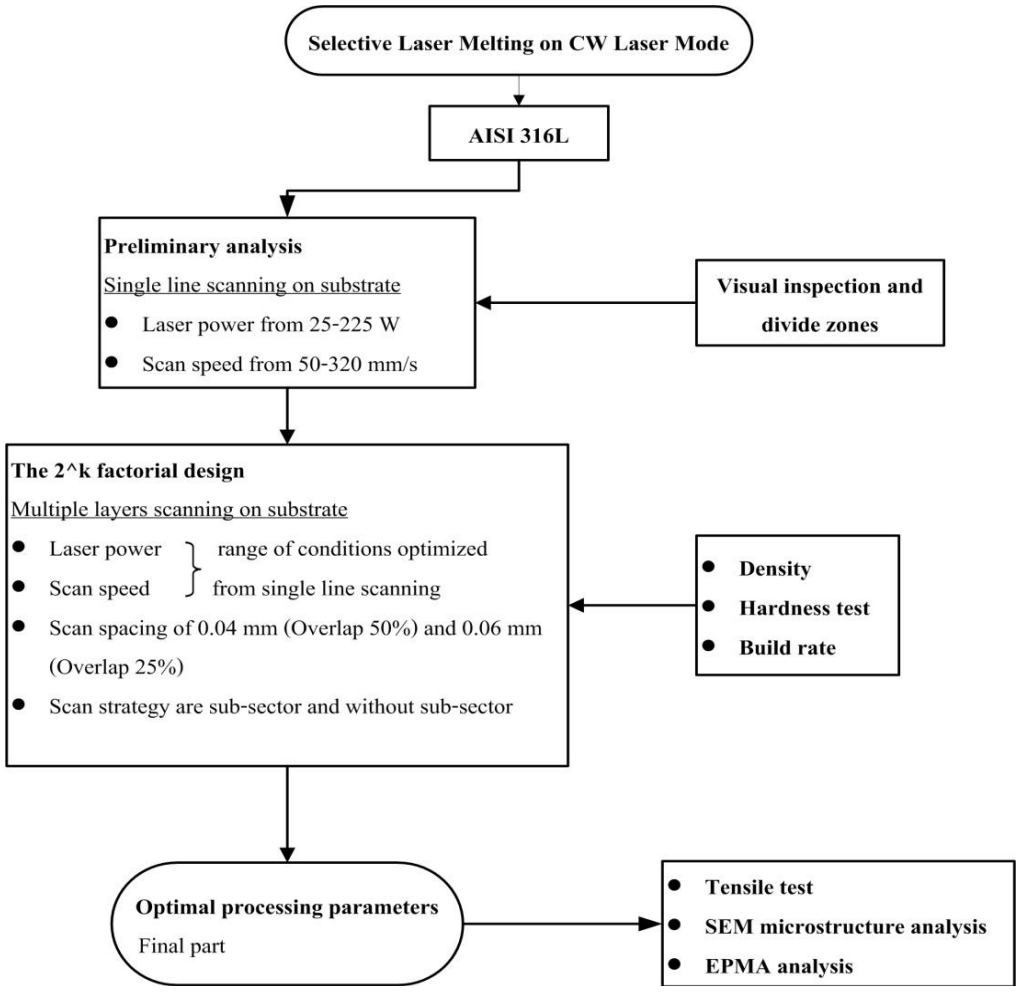

Figure 2.1: Experimental flowchart for investigating the properties of stainless steel 316L powder using SLM.

2.1.1 Setup

All experiments were performed using an in-house SLM machine (National Metal and Materials Technology Center, Thailand) as shown in Figure 2.2. The machine consisted of four main components as follows:

(1) Ytterbium fiber laser model YLR-300-SM-AC in wavelength of 1065 nm having a maximum power of 300 W and spot size of 80 μm under continuous wave mode, (2) Powder deposit system, consisting of two rectangular build platforms directly coupled to linear actuators with a minimum step size of 100 μm and controlled by a PC-based controller. Powder was delivered to the build platform using a scraper, (3) Nitrogen gas shielding system with flow rate of 10 L/min (4) Computer controller, to operate the machine and to control the laser to melt the metallic particles in each building layer. Table 2.1 illustrates the detail of the SLM machines.

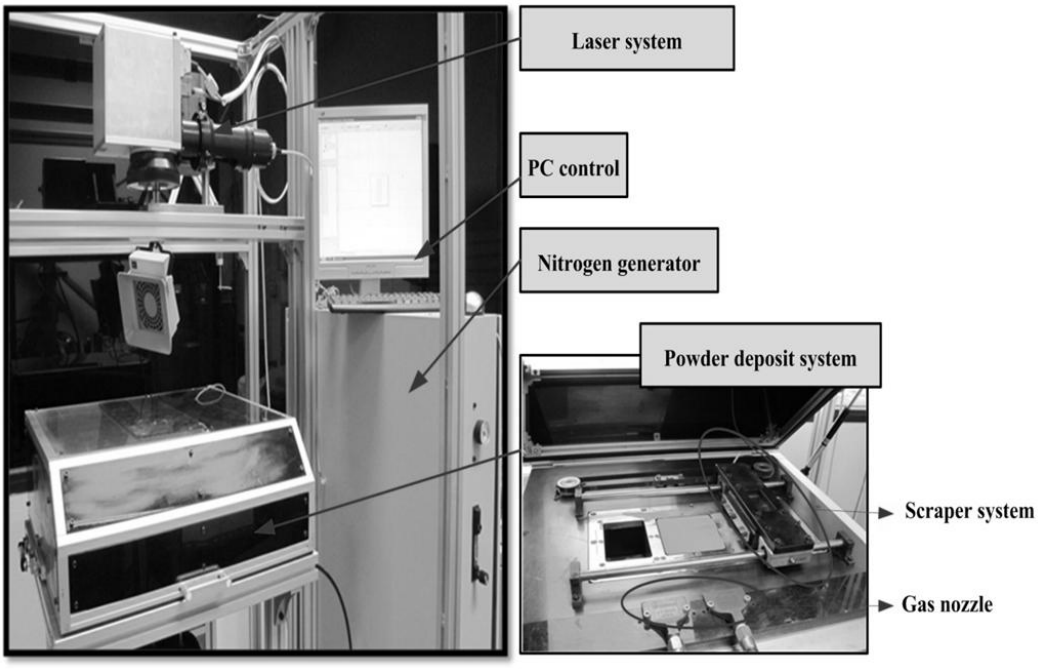

Figure 2.2: The SLM machine is developed by National Metal and Materials technology (MTEC).

Table 2.1: Specifications of the machines used for selective laser melting

Laser	Type	Fiber laser
	Wavelength	1.064 µm
	Modes	CW and Pulsed
	Maximal power on workpiece	~300 W (CW)
	Average beam diameter	~ 80 µm
	M^2 (Beam quality)	1.05
Chamber	Powder deposition system	Recoater with a scraper
	Layer deposition	Min. ~100 µm
	Build platform	100 mm x 100 mm
	Oxygen level control	Continuous gas flow

2.1.2 Powder properties

Stainless steel 316L used in the experiment was in the form of pre-alloy gas atomized powder (99% purity) for SLM process. Figure 2.3 shows the morphologies of the 316L stainless steel powders. This powder exhibits a spherical morphology and average particle size of approximately 36.6 µm. Elemental compositions of this powder are Balance Fe, 16.9% Cr, 10.9% Ni, 2.1% Mo, 1.36% Mn, 0.46% Si, 0.029% P, 0.015% S, 0.016% C. Table 2.2 shows value of some physical properties of 316L stainless steel, which will help to explain the phenomena for the optimal process parameters.

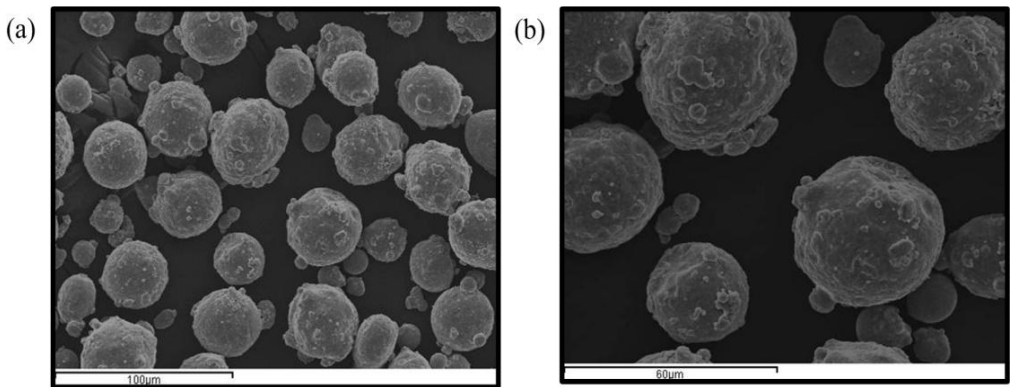

Figure 2.3 (a) The typical SEM micrograph of 316L SS particle shape and (b) an image of higher magnification.

Table 2.2: Some physical properties of bulk 316L stainless steel (Gusarov et al. 2007)

Density (ρ -kg/m^3)	4700
Melting point (T_m -K)	1,783
Latent heat of melting (L_f -J/kg)	272,500
Thermal conductivity at room temperature (λ- W/mK)	20
Specific heat at room temperature (C_p- J/kgK)	500
Reflectivity (R)	0.7

2.1.3 Preliminary analysis: Single line scanning

In order to examine the single line scanning, a 100 μm layer of the metallic power was filled over a surface area of 10 mm thick steel the substrate as shown in Figure 2.4. The line contour direction was controlled using AutoFab (Marcam Engineering GmbH, Germany) software. A 15-mm long track line scanning was performed across the powder area. Laser power and scan speed were varied in the range of 25-225 W with an incremental step of 25 W and 50-320 mm/s with a stepwise of 30 mm/s, respectively.

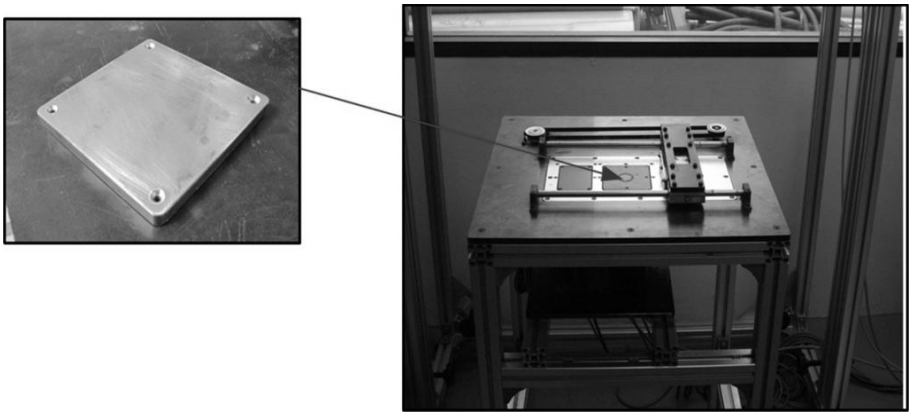

Figure 2.4: Steel substrate size 97 mm x 97 mm x 10 mm.

2.1.4 Design of experimental (DOE)

Multiple layers scanning (3D parts)

The 2^k factorial analysis was selected to optimize conditions for processing multiple layers scanning. The experiment was designed and analyzed using Minitab statistical and graphical analysis software package. The four variables including laser power, scan speed, scan spacing and scan strategy were assumed to have a linear response. Each parameter had two setting levels i.e. high (+) and low (-). The valued each variable was varied independently from each others. Among the four variables, the laser power and the scan speed is optimized from the preliminary testing whereas the scan spacing and the scan strategy will be focused in this analysis. Two scan spacing, 0.04 and 0.06 mm and two scan strategy, without sub-sector and with 5 mm rectangular sub-sector, are under consideration as shown in Figure 2.5(a) and (b) respectively. The experiment was performed by constructing 10 mm x 10 mm x 10 mm cubic parts using cross-hatched scanning strategy. The cross-hatching will remove any periodic structure that causes repetitively heating-up the same structure over each layer. Therefore, the cross-hatching helps to avoid the formation of interconnected porosity (Mumtaz, Erasenthiran, and Hopkinson, 2008).

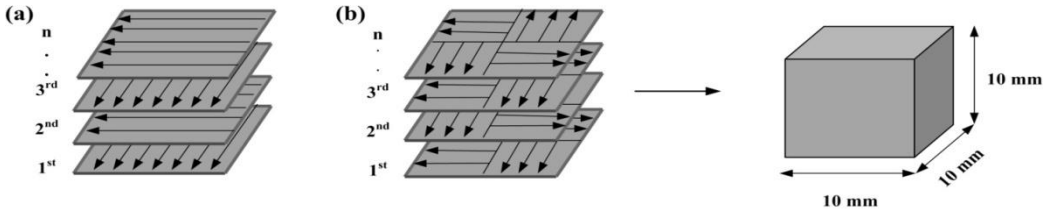

Figure 2.5: Scan strategy of fabrication 3D parts (a) without sub-sector 10 mm x10 mm (b) sub-sector 5 mm x 5 mm.

After the optimal processing parameters were obtained, standard tensile testing parts were (ASTM E8M) as shown in Figure 2.6. The parts were manufactured from the optimal processing parameters in two different orientations as see in Figure 2.7. The part in Figure 2.7(a) was built along the transversal direction, (case a) and the part in Figure 2.7(b)

was built along the longitudinal direction, (case b). To avoid overhanging problem, these parts were firstly built in a block form then wire-cut to obtain the final shape.

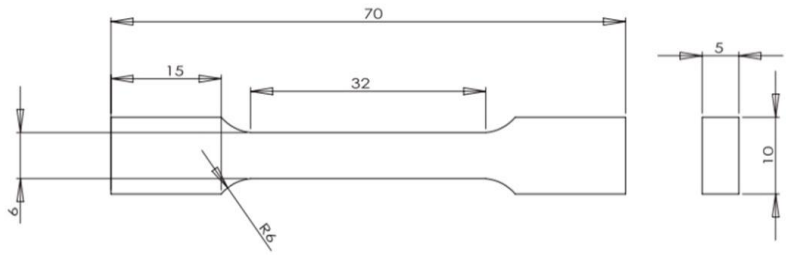

Figure 2.6: Tensile test specimen**.**

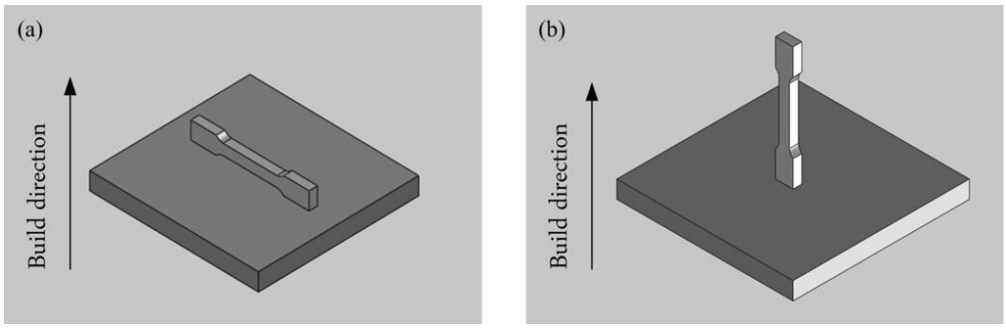

Figure 2.7: Orientation of parts of tensile test: case (a) part was build along transversal direction and case (b) part was build along longitudinal direction.

2.2 Materials Characterization

In order to analyze the quality of each parameter condition of single line scanning, the scan tracks were observed. The appearance of scan tracks can be categorized into 5 modes including un-melted, balling, smooth, irregular and over-melt as see in Figure 2.8

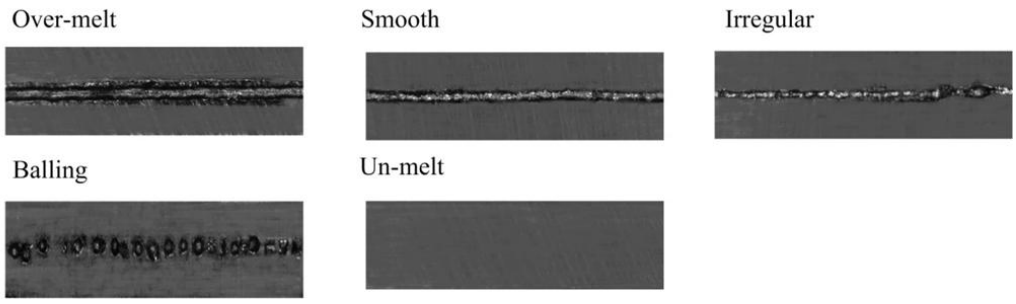

Figure 2.8: Type of scan tracks.

All multilayer parts were used to determine the density based on Archimedes' law. The hardness was also examined using Vickers micro-hardness tester and processing time was calculated in term of build rate. Subsequently, the tensile test and microstructure analysis will be performed on the optimal parts. Then, elemental composition was analyzed at the surface of the part using electron probe micro-analyzes. These testing procedures will be discussed as following:

2.2.1 Density

The densities of the SLM parts were calculated by Archimedes method (ASTM B311-93) and the relative densities were calculated based on the density of the bulk material. The test specimens were weighted using a set of AND GF-400 scales with 0.001 g accuracy as shown in Figure 2.9.

Procedure

1) Weigh the test specimen in air using an analytical balance.
2) Support the container of water below the balance for weighing specimens.
3) Suspend the test specimen support basket with the test specimen from the beam hook balance and the water should cover the specimen support basket by at least 6 mm to minimize the effect of surface tension forces on the weighing.
4) Measure the temperature of the water and record its density (E) at that temperature.
5) Weigh the test specimen and specimen support immersed in water.
6) The density is determined by calculation as equation (2.1).

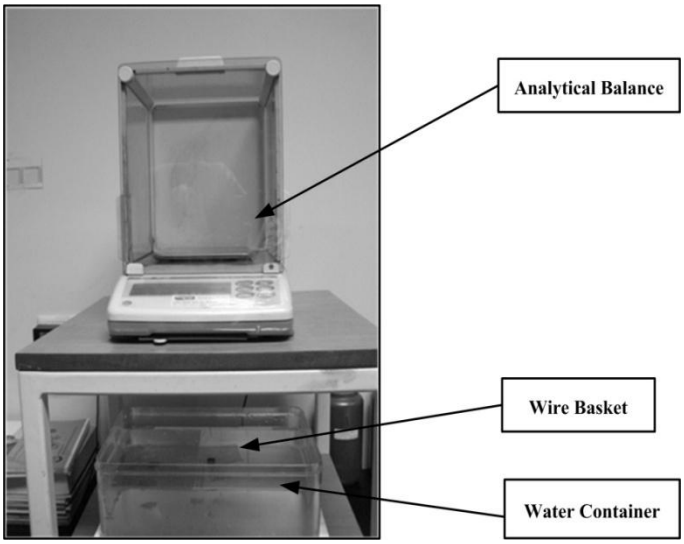

Figure 2.9: Weighing a specimen (Archimedes's law).

However, testing should be taken to ensure that the test specimen and specimen support hang freely from the balance beam hook, are free of air bubbles where immerse in the water and are at the same temperature as the water and balance. In addition, testing should to be taken to ensure that the surface of the water is free of dust particles (dirt, grease, oil, oxide scale, metal powders or assembly materials.

The calculation of the density is as follow:

$$D = (A \times E)/(A - B + C) = (A \times E)/(A - F) \quad (2.1)$$

Where: D = density of test specimen, g/cm^3

A = mass of test specimen in air, g

B = apparent mass of test specimen and specimen support in water, g

C = mass of specimen support immersed in water, g

F = mass of test specimen in water with mass of specimen support tared, g and

E = density of water in g/cm^3

2.2.2 Vickers micro-hardness testing

The hardness of 32 specimens of 316L stainless steel SLM parts were determined using Vickers micro-hardness test (ASTM C1327-03) with a Microhardness Tester (Anton-Paar, MHT-10) having testing procedure as follows:

1) The surface of specimens has to be prepared surface before testing by simply embedding the specimens a thermo-hardening polymer as see in Figure 2.10.
2) Parts are ground with five different grades of SiC paper: P240, P800, P1200, P2600, P4000 and polished using two different grades of polishing cloth: 3 μm and 1 μm respectively.
3) Hardness was measured by applying load of 400 g for 15 s. Indentation locations were indentified using 3x3 grid with a distance of 2.5 mm between each location Fig 2.10.

In testing, the pacing of indentations should be at least four time the diagonal lengths between the centers of the indentations. If there is cracking from the indentations, the spacing shall be increased to at least five times the length of the cracks.

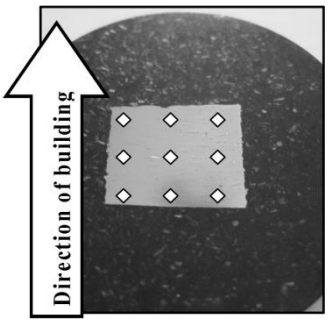

Figure 2.10: The preparing part for hardness test.

2.2.3 Tensile testing

The tensile testing was carried out on a Universal Testing Machine (Instron Model 55R4502) mechanical as shown in Figure 2.11. Both ends of the test specimens were gripped using jaws and manually aligned to be parallel to the vertical axis of the machine. The

tests were performed using a cross speed of 10 mm/min and the stress-strain curve of each test obtained from an average of at least five specimens.

Figure 2.11: Universal Testing Machine (Instron Model 55R4502).

2.2.4 Microstructure analysis

The standard methods were used for metallographic part preparation: embedding the specimen in a thermo-hardening polymer, grinding with SiC paper: P240, P800, P1200, P2600, P4000 respectively and polishing with a 3 μm and 1 μm diamond suspension using Polishing Machine (Struers Model Rotopol 25). Then, the specimens were etched by electrolytic etching with Glycerol 3 vol%, Hydrochloric acid 2-5 vol% and nitric 1 vol% at 6-12 V dc for 5-10 seconds (ASM 9). Finally, the microstructure is analyzed on a ZEISS Reflected light Microscope Axiotech 100H with Image Pro Plus (Media Cybernetics version 5.1) and scanning electron microscope (SEM) model JSM-5410 (JEOL).

2.2.5 Electron probe micro-analyzer (EPMA)

The specimens were prepared using the same procedure as presented in microstructure analysis. The parts are ground and polished to 1 μm. However, the embedding should be mounts up to 1 inch in diameter to use in stable of 1.4 x 10^{-5} Pa vacuum environment and under electron bombardment. After preparation, the specimens were coated with an approximately 200 Angstrom (10 nm) layer using a gold conductive material.

The electron probe micro-analyzer model 1610 (Shimadzu) of MTEC is used in this experiment. The line scanning having a length of 512 mm was performed under conditions of electron beam size 5 μm, beam current 0.05 μA and part current 0.03 μA to observe elemental composition of each layers. Afterward, the quantification was performed with software which considers excitation with electrons and carries out the data correction of the matrix.

CHAPTER 3

Results and discussion

3.1 Preliminary testing: Single line scanning

The result of single line scanning is shown in Figure 3.1, a parametric dependent overview of the mechanisms of single line laser scanning on based plate. It can be divided into five different zones; un-melt, smooth, balling, irregular and over-melt, according to different laser powers and scan speeds.

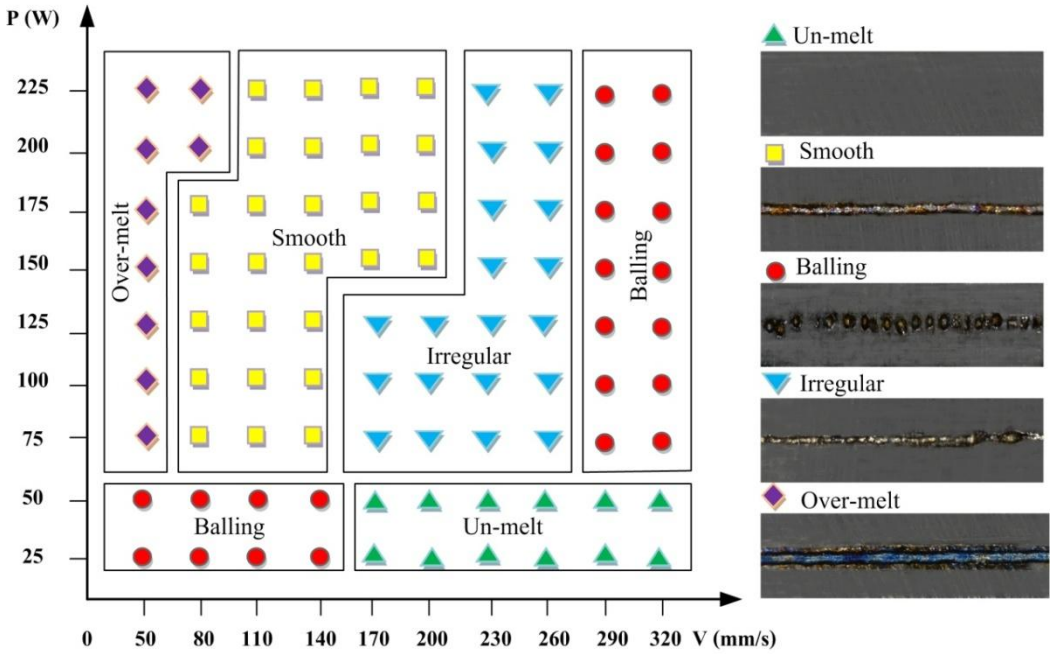

Figure 3.1: Line scans on a substrate at room temperature (scheme).

It can be noticed from Figure 3.1 that the "un-melt tracks" appeared where the laser power is lower than 50 W. At this stage, the energy generated from the laser is insufficient to melt the metallic particles. Therefore, each particle individually remained un-melt this condition. The "balling tracks" occurs under two scanning conditions: condition (A) at relatively low laser

power (25-50 W) and scan speed ranging from (50-140 mm/s), and condition (B) at high laser power (75-225 W) and scan speed above 290 mm/s. It can be obviously seen that liquid-solid mixture (melt pool) having high viscosity is a consequence at condition (A). In contrary, the molten track is formed at condition (B) under the scan speed above 290 mm/s and high enough laser power deposition. The spherical droplets occurred in line scanning when the atmosphere during processing has high oxygen content. As a consequence, liquid tries to reduce surface energy by forming small balls. In addition, some energies are released due to the exothermic reaction from oxidation which leads to a higher instability of the melt pool (Rombouts 2006; Yadroitsev, Bertrand, and Smurov, 2007).

The "smooth tracks" can be formed by laser power and scan speed in the range of 75-225 W and 80-200 mm/s, respectively. This phenomenon can be described as sufficient liquid stability, continuous-and-smooth melted tracks without balling formation. The "irregular tracks" is caused by high scan speed (170-260 mm/s) and high laser power (75-225 W). The appearance of track is generally distorted and un-continued. This is subsequent of reduction in surface energy and instability of liquid.

The "over-melt tracks" is normally overheating, oxidation and tracks widening which subsequently presented as large melt pool. This generally occurs at low scan speed and high laser power (Mumtaz, Erasenthiran, and Hopkinson 2008; Gu and Shen 2009; Yadroitsev, Bertrand, and Smurov, 2007).

3.2 Design of experimental analysis (DOE): Multiple layers scanning

The results of this experiment were statistically analyzed using Minitab software program. The optimal condition of the single line scanning was used to build the cube for multiple layers scanning at the laser powers and scan speed were 75 W, 175 W and 80 mm/s, 200 mm/s, respectively. The parameters for multi-layers scanning test were designed using 2^4 factorial designs as shown in Table 3.1. Thus all experiments had 16 conditions and each condition is replicated for two times. All cubes were examined density, hardness and build rate as shown in Table 3.2 and Figure 3.2 shows the multi-layer scanning parts on 16 different conditions.

Table 3.1: Variable symbols and level setting

		Levels	
Variable	Symbol	Low (-)	High (+)
Laser power (W)	P	75	175
Scan speed (mm/s)	V	80	200
Scan spacing (mm)	Ss	0.04	0.06
Scan strategy (mm)	S	5 (sub-sector)	10 (without sub-sector)

Table 3.2: The 2^4 factorial showing the choice of parameters, their respective levels, and the corresponding response parametric values

Exp. No.	**n**	**Input parameters**				**Response parameters**		
		P	**V**	**Ss**	**S**	**Density (%)**	**Hardness (HV)**	**Build rate (cm^3/hr)**
1	1	75	200	0.04	10	80.03	208.42	1.85
	2	75	200	0.04	10	82.77	208.46	1.85
2	1	175	200	0.04	10	97.75	219.50	1.85
	2	175	200	0.04	10	97.40	219.87	1.85
3	1	75	200	0.04	5	86.09	212.15	1.87
	2	75	200	0.04	5	85.87	211.71	1.87
4	1	175	200	0.04	5	97.90	229.13	1.87
	2	175	200	0.04	5	99.30	227.70	1.87
5	1	75	80	0.04	10	90.50	208.34	0.93
	2	75	80	0.04	10	88.09	208.97	0.93
6	1	175	80	0.04	10	99.01	227.66	0.93
	2	175	80	0.04	10	97.31	228.26	0.93
7	1	75	80	0.04	5	92.36	213.30	0.95
	2	75	80	0.04	5	92.23	214.15	0.95

Table 3.2: The 2^4 factorial showing the choice of parameters, their respective levels, and the corresponding response parametric values (continued)

Exp. No.	n	Input factors				Response parameters		
		P	V	S_s	S	Density (%)	Hardness (HV)	Build rate (cm^3/hr)
8	1	175	80	0.04	5	99.21	226.29	0.95
	2	175	80	0.04	5	99.30	225.21	0.95
9	1	75	200	0.06	10	80.04	202.02	2.58
	2	75	200	0.06	10	83.92	203.30	2.58
10	1	175	200	0.06	10	88.93	216.14	2.58
	2	175	200	0.06	10	88.47	215.94	2.58
11	1	75	200	0.06	5	87.77	209.91	2.39
	2	75	200	0.06	5	87.64	209.00	2.39
12	1	175	200	0.06	5	98.98	223.49	2.39
	2	175	200	0.06	5	97.69	222.53	2.39
13	1	75	80	0.06	10	91.00	214.40	1.47
	2	75	80	0.06	10	89.48	215.15	1.47
14	1	175	80	0.06	10	96.00	226.39	1.47
	2	175	80	0.06	10	99.62	226.96	1.47
15	1	75	80	0.06	5	93.10	214.75	1.50
	2	75	80	0.06	5	92.07	214.44	1.50
16	1	175	80	0.06	5	95.10	222.06	1.50
	2	175	80	0.06	5	95.25	221.33	1.50

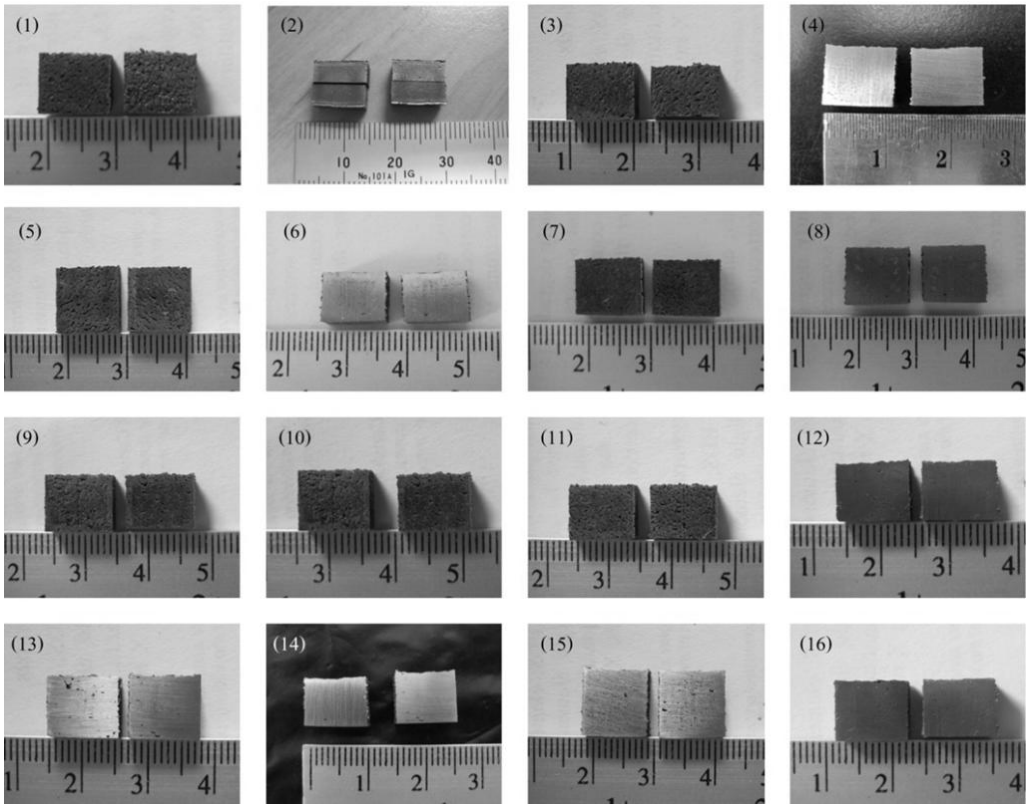

Figure 3.2: Selective laser melting specimens named as per experiment number in the factorial design in Table 3.2.

Subsequently, all data are analyzed using (ANOVA) table to estimate effects in decreasing order of magnitude for parameters both individually and combined. The p-value represented the 95% confidence level, thus p-value beyond the effects that are statistically significant. In this experiment, the analysis of variances (Table 3.3) shows that the 9 effects are statistically significant for the density. The single most influential fabrication parameters are P, V, S and Ss respectively. The interactions of fabrication parameters are significant including P·V, V·S, P·Ss, P·Ss·S and P·V·Ss·S. For hardness can be see that all 13 effects are statistically significant, except the three interaction of P·Ss·S. Moreover, the main effects of V, Ss and interaction effects of V·Ss are considered that these parameters have directly influence on build rate. Next section is discussed about effect of main parameters and effect of interaction parameters.

ANOVA Table

Full Factorial Design

Factors: 4 Base Designs: 4, 16

Runs: 32 Replicates: 2

Table 3.3: Analysis of variances for density, hardness and build rate

Source	Density (%)				Hardness (HV)				Build rate (cm^3/hr)			
	df	**Seq SS**	**F**	**p**	**df**	**Seq SS**	**F**	**p**	**df**	**Seq SS**	**F**	**p**
P	1	650.34	401.70	**0.000**	1	1377.99	4424.05	**0.000**	-	-	-	-
V		149.13	92.11	**0.000**	1	146.16	469.25	**0.000**	1	7.37	2730.67	**0.000**
Ss	1	12.58	7.77	**0.013**	1	30.63	98.35	**0.000**	1	2.74	1014.00	**0.000**
S	1	76.69	47.37	**0.000**	1	70.12	225.13	**0.000**	-	-	-	-
P·V	1	50.80	31.38	**0.000**	1	2.35	7.54	**0.014**	-	-	-	-
P·Ss	1	36.59	22.60	**0.000**	1	21.53	69.13	**0.000**	-	-	-	-
P·S	1	5.33	3.29	0.088	1	5.55	17.83	**0.001**	-	-	-	-
V·Ss	1	1.66	1.02	0.327	1	44.91	144.19	**0.000**	1	0.01	4.74	**0.038**
V·S	1	36.81	22.74	**0.000**	1	100.01	321.07	**0.000**	-	-	-	-
Ss·S	1	3.61	2.23	0.155	1	5.24	16.83	**0.001**	-	-	-	-

Table 3.3: Analysis of variances for density, hardness and build rate (continues)

Source	Density (%)				Hardness (HV)				Build rate (cm^3/hr)			
	df	**Seq SS**	**F**	**p**	**df**	**Seq SS**	**F**	**p**	**df**	**Seq SS**	**F**	**p**
P·V·Ss	1	4.18	2.58	0.128	1	16.63	53.40	**0.000**	-	-	-	-
P·V·S	1	6.55	4.05	0.061	1	38.26	122.83	**0.000**	-	-	-	-
P·Ss·S	1	2.41	1.49	0.240	1	0.84	2.68	0.121	-	-	-	-
V·Ss·S	1	24.99	15.44	**0.001**	1	11.44	36.72	**0.000**	-	-	-	-
P·V·Ss·S	1	13.89	8.58	**0.010**	1	7.12	22.85	**0.000**	-	-	-	-
Error	16	25.90	-	-	16	4.98	-	-	28	0.08	-	-
Total	31	1101.45	-	-	31	1883.77	-	-	31	10.19	-	-
	R-Sq (adj) = 95.44%,				R-Sq (adj) = 99.49%				R-Sq (adj) = 99.18%			

Where: DF = Degree of Freedom, Seq SS = Sequential Sum of Squares, F = f-test value, p = P-value and R-Sq = The Coefficient of Determination

The main effect plot

A main effects plot is represented the average responses, which obtain for parts and the specific parameter level do not depend on other variable settings. The line represents the magnitude (positive or negative) effect of changing the individual parameter. The first analysis is laser power which has an influence with density and hardness as shows in table 3.3, indicating a significant effect p = 0.000. Figure 3.3(a) shows that increasing of laser power from 75-175 W leads to increase density approximately 10.27%. Due to increasing of laser power can increase temperature of melting while low laser power does not generate enough heat to fully melt powder. Figure 3.3(b) observes that the effect of laser power in terms of part hardness increase approximately 6.23% when laser power is increased values. As a consequence, it is believed that hardness is proportional to density. For build rate, effects of laser power have no significant and then the line remains constant when laser power is increased as shows in Figure 3.3(c).

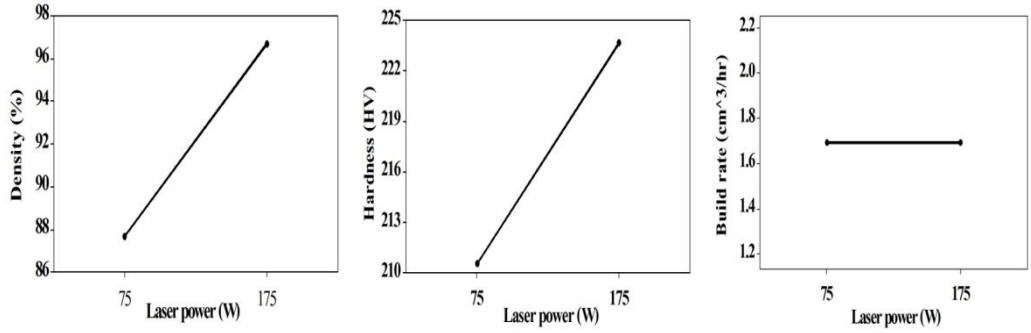

(a) (b) (c)

Figure 3.3: Main effects plot (data means) for response (a) density, (b) hardness and (c) build rate with respect to laser power**.**

The results in Figure 3.4(a) and (b) show that scan speed can decrease density and hardness of parts are 4.8% and 2% respectively when it is increased from 80 – 200 mm/s. In contrast, build rate increases approximately 85% as shows in Figures 3.4(c). These results can be understood by considering the melting temperature and attendant heat effect zone, which is caused by laser energy. Thus, increasing scan speed with other

parameters constants cause a lower melting temperature and, accordingly, a smaller amount of liquid formation, as evidence in a smaller molten pool size (Ruidi et al. 2010; Mumtaz, Erasenthiran, and Hopkinson, 2008). In addition, when scan speed is reduced, the energy for melted powder is increased and build rate is reduced.

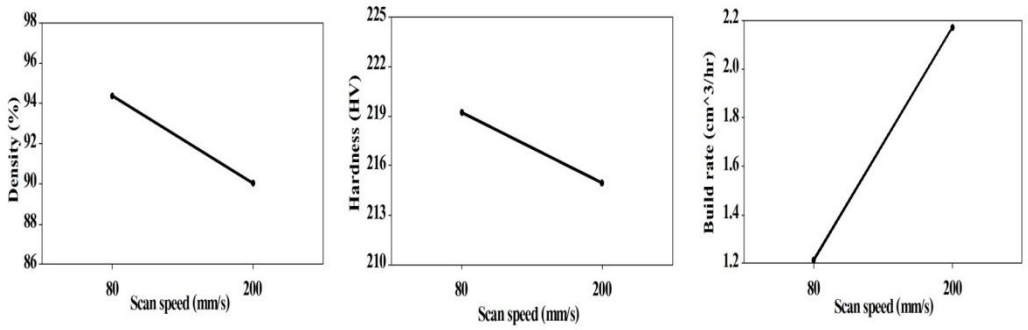

(a) (b) (c)

Figure 3.4: Main effects plot (data means) for response (a) density, (b) hardness and (c) build rate with respect to scan speed.

The density and hardness of parts decrease approximately 1.3% and 1% after scan spacing is varied from 0.04-0.06 mm as shows in Figure 3.5 (a) and (b). It can be understood that the beam will not pass over the same area several times when scan spacing is increased. Therefore, the line of melted beads is not remains homologous temperature and the heat cannot penetrate deeper into the powder bed. Whereas, increasing of scan spacing can increase build rate of 42% as shows in Figure 3.5 (c). It is noticed that effect of scan spacing on build rate is similar effect of scan speed because at high scan spacing can reduce distance of scanning also.

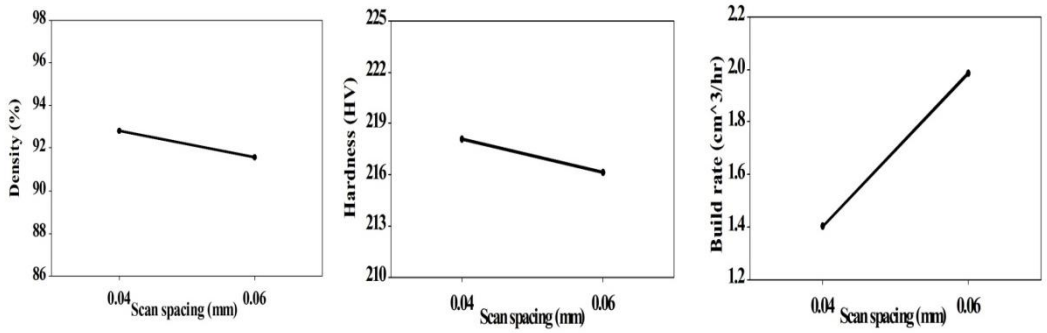

(a) (b) (c)

Figure 3.5: Main effects plot (data means) for response (a) density, (b) hardness and (c) build rate with respect to scan spacing.

Figure 3.6 (a) and (b) observe that the density and hardness decrease about 3.4% and 1.4% at scan strategy is increased from 5-10 mm. These results can explain that due to the short scanning length causes the melted temperature of previous adjacent scan line remains high and have short cooling period. Meanwhile, the without sub-sector strategy have long scan tracks thus low temperature leads to the worse wetting and low density (Simchi 2003; Kruth et al., 2004). Figure 3.6 (c) can be observed that the both of scan strategy are less significant on build rate. The sub-sector strategy has manufacturing time less than sub-sector strategy because overlapping of each sub-sector is not scanned as shows in Figure 3.7 (a). Therefore, the distance each layer of sub-sector strategy is less than without sub-sector strategy (Figure 3.7(b)) approximately 231 mm. Indeed, sub-sector strategy has on and off laser and idle distance during process more than without sub-sector strategy. For this reason, the sub-sector scanning has manufacturing time lower than without sub-sector strategy. If the both scan strategy have the same distance scanning. Consequently, these results can support that the scan strategy should be performed the sub-sector scanning.

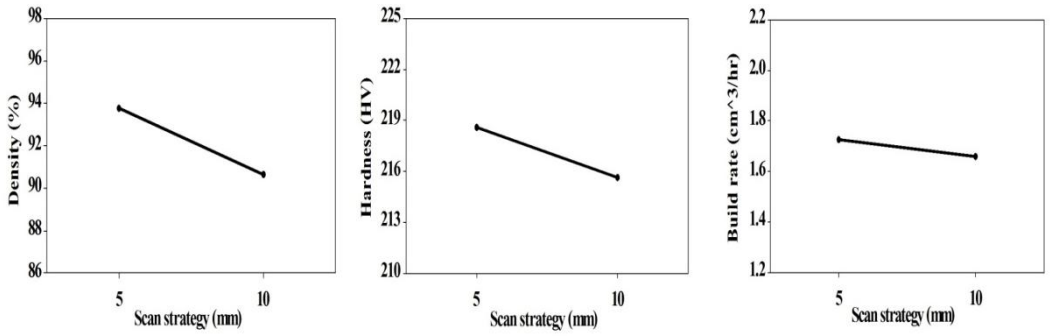

(a) (b) (c)

Figure 3.6: Main effects plot (data means) for response (a) density, (b) hardness and (c) build rate with respect to scan strategy.

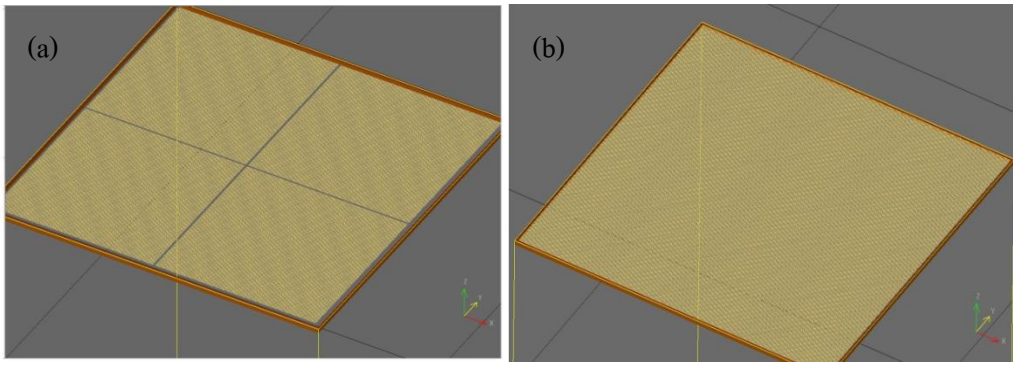

Figure 3.7: Area of scanning (yellow shading) into each layer thickness by (a) sub-sector strategy and (b) without sub-sector strategy.

The interaction effect plot

Due to it is possible that the interaction of parameters may have significant more important the effect of a single factor. The interaction plot represents the average of response obtains for parts built. The two parameter settings do not depend on the other variables. Then, the interaction effects on density, hardness and build rate are also studied. This section shows significantly interaction effect as results in Table 3.3 (p-value > 0.05). Figure 3.8 (a) can observe that the interaction of laser power and scan speed have influence with part density. There are increasing of scan speed and decreasing of laser power lead to insufficient energy for melted powder. This result can be seen in Figuer 3.8 (b) which shows

the part density tends to decrease when scan speed is increased from 80-200 mm/s but laser power is fixed. In additon, the result of hardness is found that interaction between laser power and scan speed have less significant. This result is agreed with the ANOVA analysis (Table 3.3).

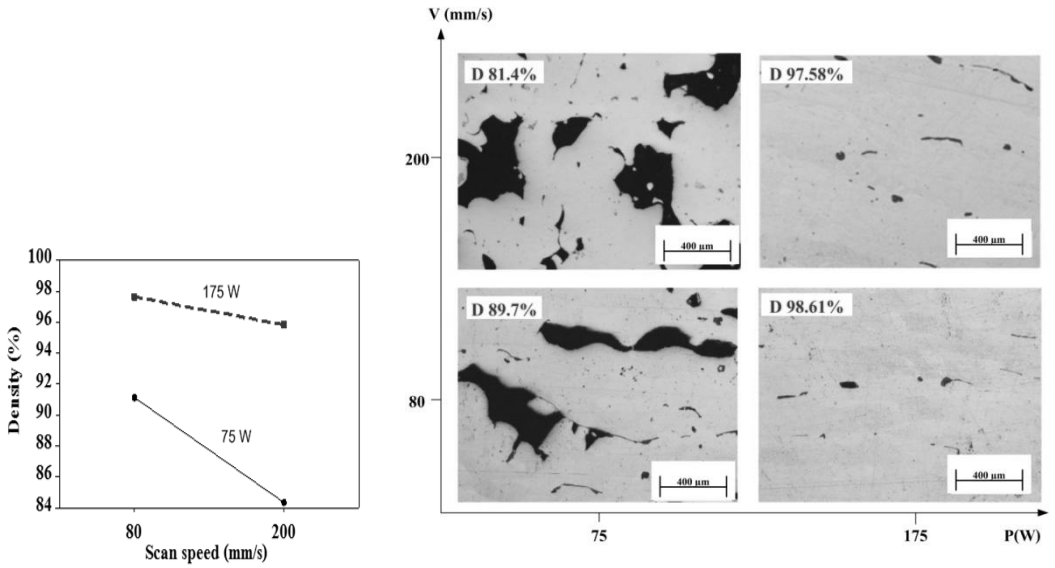

(a) (b)

Figure 3.8: (a) Interaction effect plot for density (%) with respect to laser power and scan speed and (b) Micrographs shows part density for the four parameter settings by varying laser power and scan speed at scan spacing 0.04 mm and scan strategy 10 mm constant.

The interaction between laser power and scan spacing with respect to part density and hardness as shows in Figure 3.9 (a) and (b). It can observe that decreasing of laser power and increasing of scan spacing have less difference for density and hardness. This result is possible that temperature distribution and the existence time of the melt pool are still not enough. Meanwhile, the high laser power 175 W can observe that density and hardness trend to increase as shows in Figure 3.10. Therefore, these results can indicate that interaction between the laser power and the scan spacing is significant for density and hardness.

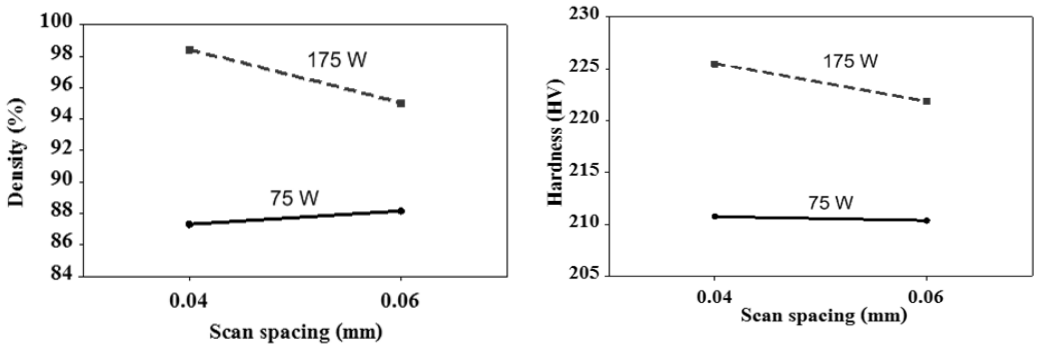

(a) (b)

Figure 3.9: Interaction effect plot for (a) density (%) and (b) hardness (HV) with respect to laser power and scan spacing.

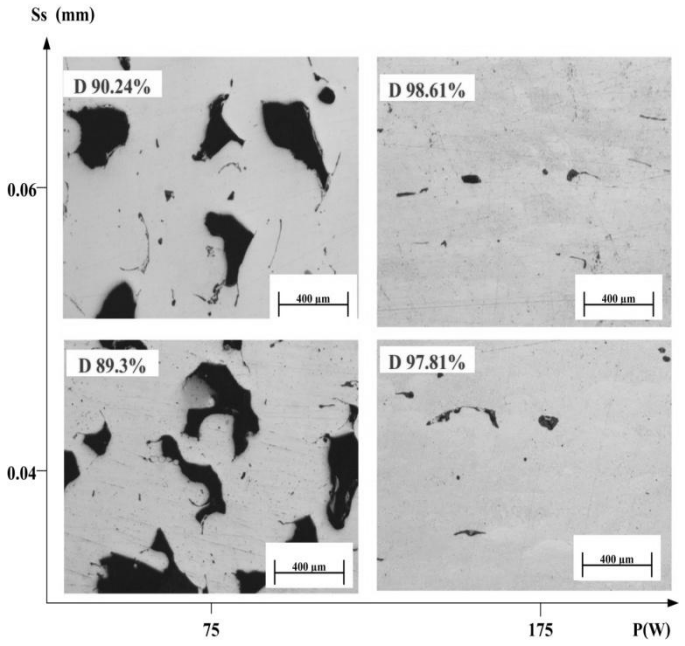

Figure 3.10: Micrographs were shown part density for the four parameter settings by varying laser power and scan spacing at scanning speed 80 mm/s and scan strategy 10 mm constant.

Figures 3.11 (a) shows that the interactions between scan speed and scan spacing is a significant with hardness. This result occurs due to the large scan spacing and high scan speed causes the total energy impart on the powder layer decreases and leads to increasing of porosity. Therefore, scan speed and scan spacing should be decreased to decrease porosity and increase hardness. In addition, the decreasing scan spacing can improve irregularly surface (Van Elsen, 2007). However, Figure 3.11 (b) shows interaction

between scan speeds and scan spacing with regard to build rate. It is found that lines almost parallel which mean that laser power and scanning speed have a less significant with build rate because of the main effect (scan speed and scan spacing) are large effects on build rate (Rombout, 2007).

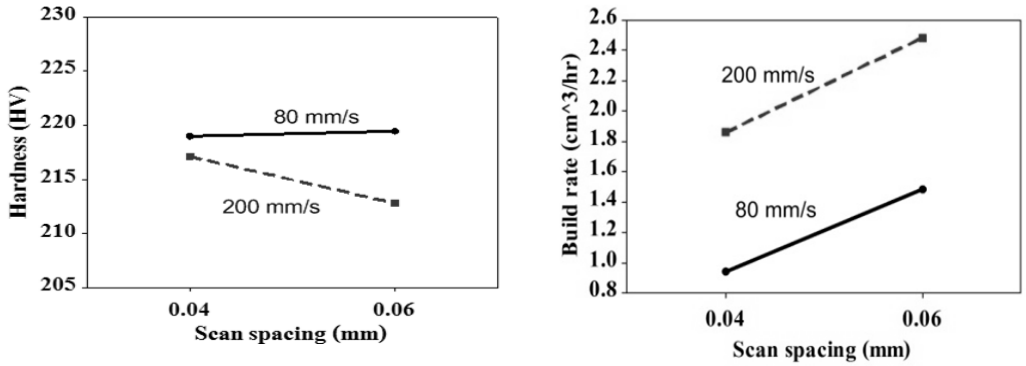

(a) (b)

Figure 3.11: Interaction effect plot for (a) hardness and (b) build rate with respect to scan speed and scan spacing.

Figure 3.12 (a) indicates that interaction of scan speed and scan strategy has influence with density. It can ascribe that at low scan speed and sub-sector scanning has the high energy, which is delivered to melt of the powder. Thus it can ensure sufficient bonding between adjacent layer scan tracks as the result is shown high denes 99.25% in Figure 3.13. Besides, the interaction effect between scan speed and scan spacing is found that the lines almost crossing and that have significant with hardness as shows in Figure 3.12(b). Due to scan strategy of 10 mm used time of longer cooling period sub-sector 5 mm thus the hardness values tend to lower.

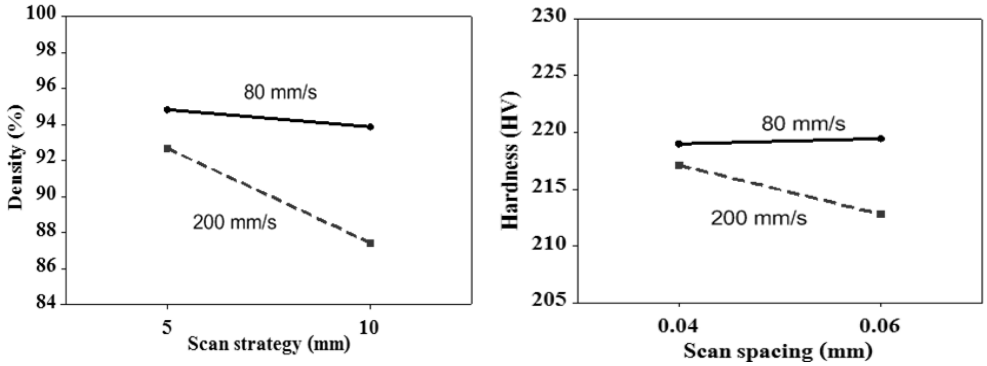

(a) (b)

Figure 3.12: Interaction effect plot for (a) density and (b) hardness with respect to scan speed and scan strategy.

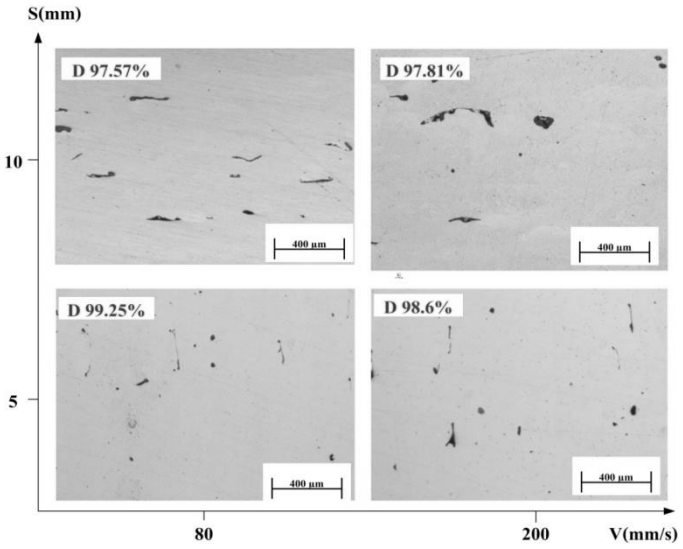

Figure 3.13: Micrographs were shown part density for the four parameter settings by varying scan speed and scan strategy at laser power 175 W and scan spacing 0.04 mm constant.

However, the interaction effects of parameters still have some of interaction which is not explained in this experiment. Especially, interaction effects of three and four parameters due to it have less statistical significant when is compared with main effect and interaction effect of two parameters as sum of square values as shows in Table 3.3. This result corresponds with several authors have ever reported that laser power, scan speeds, scan spacing and scan length are the main affecting parameters (Li et al., 2009; Morgan et al., 2004; Yadroitsev et al., 2007).

Model adequacy checking of experiment

This section is residuals examination to check model adequacy of the results as shows in Table 3.2. Also, the normal distribution, histogram, residual versus fits and residual versus order are plotted for responses (density, hardness and build rate) as shows in Figure 3.14, 3.15 and 3.16 respectively. This is formal statistical procedures for detecting inspection. A rough check for outlines is made by examining standardized residual that if the errors $\in_{ij}$ are N $(0, \sigma^2)$. The standardized residuals should be approximately normal with mean zero and unit variance. Thus about 68 percent of the standardized residual should fall within the limits ±1, about 95 percent of them should fall within ±2 and virtually all of them should fall within ±3. A residual bigger than 3 or 4 standard deviations from zero is a potential outlier (Montgomery, 1991).

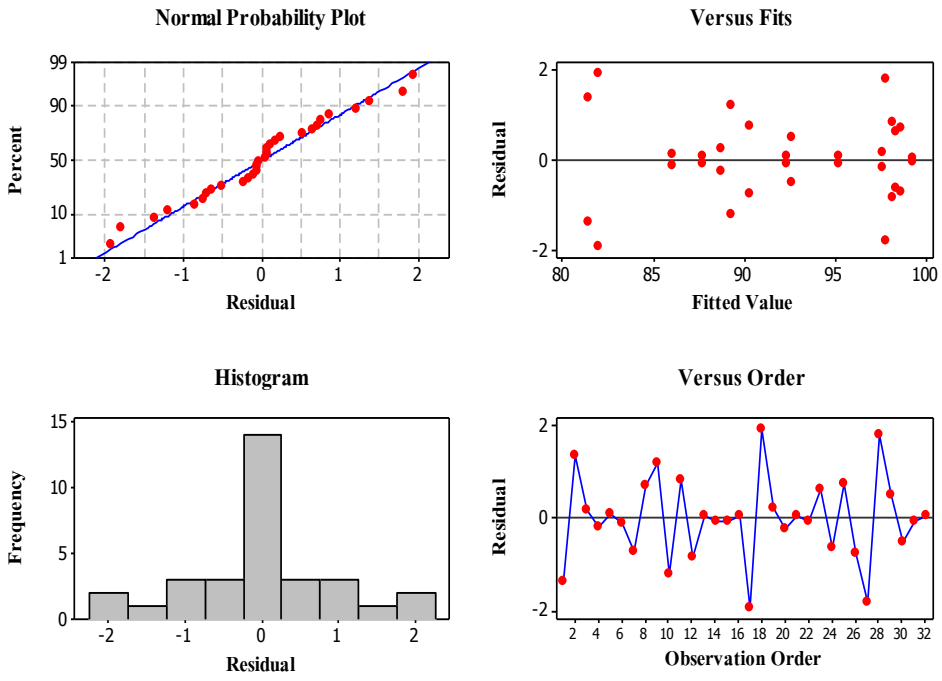

Figure 3.14: Residual plots of density (%).

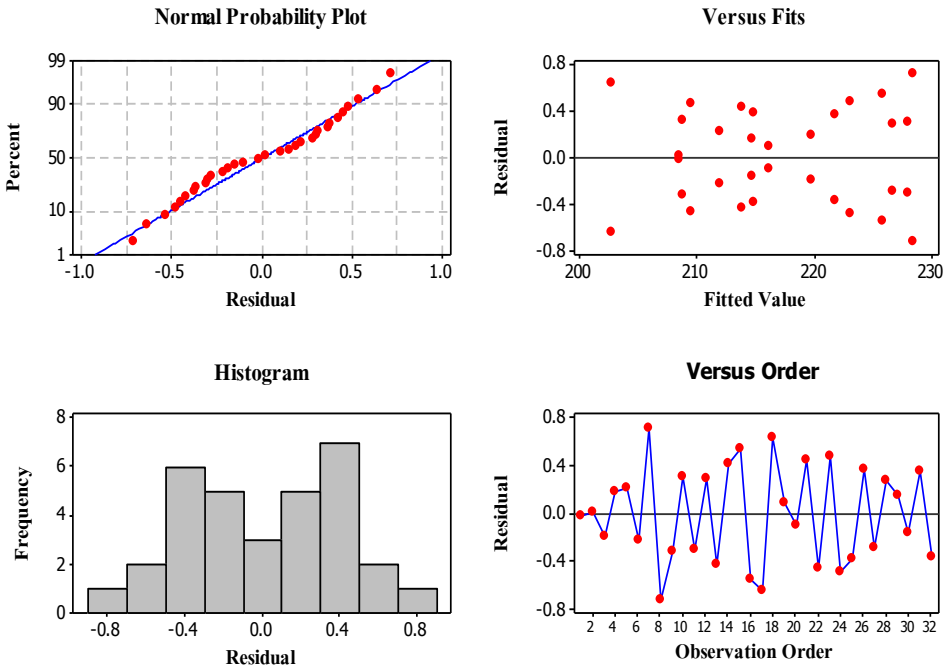

Figure 3.15: Residual plots of hardness response (HV).

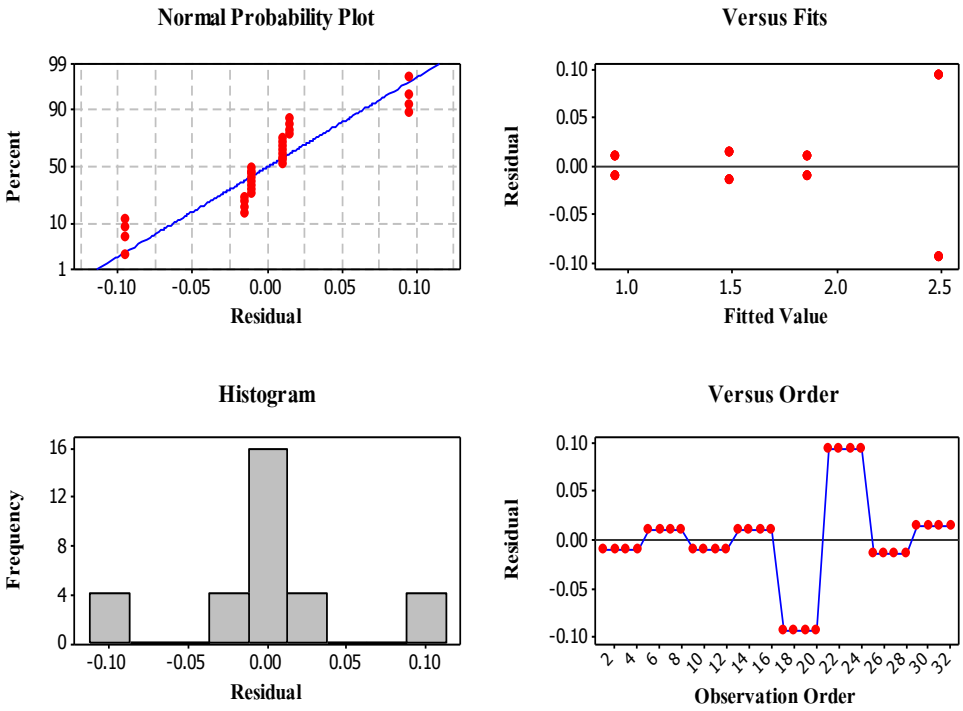

Figure 3.16: Residual plots of build rate response (cm^3/hr).

Figure 3.14 observes the normal probability plot which has the data points on probability plot close to the straight line and the histogram have a symmetric, bell shape. Both indicate that the data not show any unusual features. For the graph of residuals versus fitted and residuals versus order can observe that the residuals on the vertical axis and the on the horizontal axis have independent variable. In addition, the residual values still fall within the limits ±2. Meanwhile, Figure 3.15 and 3.16 shows the normal probability and the histogram plot for response hardness and build rate. These residuals plot support that the distribution of the data obtains for both responses are normal. Even though, the normal probability plot of build rate has some of residual a point on probability plot. It not closes to the straight line but when the histogram, the plot of residual versus fit and residual versus order is observed. It can support that the residual values have normal and random pattern. Therefore, these residuals plot are concluded that the data has normal and random pattern, indicating a good fit for a linear model. Consequently, the linear equations are estimated the final model for the response variable of density, hardness and build rate as follows:

Density (%) = 92.19-4.51(P)+2.16(V)+0.63(Ss)+1.55(S)+1.3(P)(V)-1.07(P)(Ss) +0.4(P)(S)- 0.23(V)(Ss)-1.07(V)(S) 0.34(Ss)(S)+0.36(P)(V)(Ss)+ 0.45(P)(V)(S)+0.27(P)(Ss)(S)+ 0.88(V)(Ss)(S) -0.66(P)(V)(Ss)(S) (3.1)

Resulting in R^2 = 95.44%. Some interactions seem to have no certain effect on the result (p > 0.50), indicating that these interactions might be omitted.

Hardness (HV) = 217.09-6.56(P) +2.14(V)+0.98(Ss)+1.48(S)+0.27(P)(V)- 0.82(P)(Ss) +0.42(P)(S) -1.19(V)(Ss)-1.77(V)(S)+0.40(Ss)(S)- 0.72(P)(V)(Ss) + 1.09(P)(V)(S) + 0.59(V)(Ss)(S)+0.47(P)(V)(Ss)(S) (3.2)

Resulting in R^2 = 99.49%. The interactions have certain effect on the result (p > 0.50), indicating that these interactions should not be omitted.

Build rate (cm^3/hr) = 1.69 - 0.48(V) - 0.29(Ss) + 0.02(V)(Ss) (3.3)

Resulting in R^2 = 99.18%. The interactions have certain effect on the result ($p > 0.50$), indicating that these interactions should not be omitted.

Response Optimizer – Factorial

According to 2^k factorial design, the optimization of a system was achieved by MINITAB setting. The levels of the parameters were determined the desired levels of the output parameters. Subsequently, all data were optimized by desirable determination including density of 97% - 100%, micro-hardness of 220 HV-250 HV and build rate of 0.93 cm^3/hr-2.58 cm^3/hr as shows in Appendix A9. It is found that the optimal condition is laser power 175 W, scan speed 200 mm/s, scan spacing 0.04 mm, and scan strategy 5 mm (sub-sector). This condition can build parts, which have density 98.6% and hardness 228 HV. The results of this experiment reveals that density of final parts likely increase when laser power is higher than 175 W. However, most of the previous studies is carried out with laser power in a range of 25-200 W and scan speed in a range of 20-300 mm/s (Li et al. 2009-2010; Yadroitsev, Bertrand, and Smurov 2007). Due to fiber laser system is high power laser and has high absorption for metal. Thus, when powder is melted at high laser power it is possible that the melted pool may occurs vaporization during melting. Moreover, many authors found that percent scan spacing should be less than 50% to increase density and smooth surface. (Morgan et al., 2001; Kruth et al., 2003; Gu et al., 2006). Meanwhile, Kruth et al., 2004 and Osakada et al., 2006 reported that sub-sector strategy or short scanning helped to reduce different temperature which can cause distortion, cracking and shrinkage. Therefore, the optimal condition of this experiment is laser power 175 W, scan speed 200 mm/s, scan spacing 0.04 mm, and scan strategy 5 mm (sub-sector).

3.3 Mechanical properties

The tensile parts were manufactured in two different orientations as shown in Figure 3.17(a) and (b). The parts in Figure 3.17(a) were built along transversal direction (case (a) in section 2.1.4) while the parts in Figure 3.17(b) were built along longitudinal direction

(case (b) in Section 2.1.4). It is found that the tensile strength (σ_u) of both cases is 475 MPa and the yield strength σ_y of case (a) is higher than that of case (b). However, elongation of case (a) is lower than that of case (b) as shows in Table 3.4.

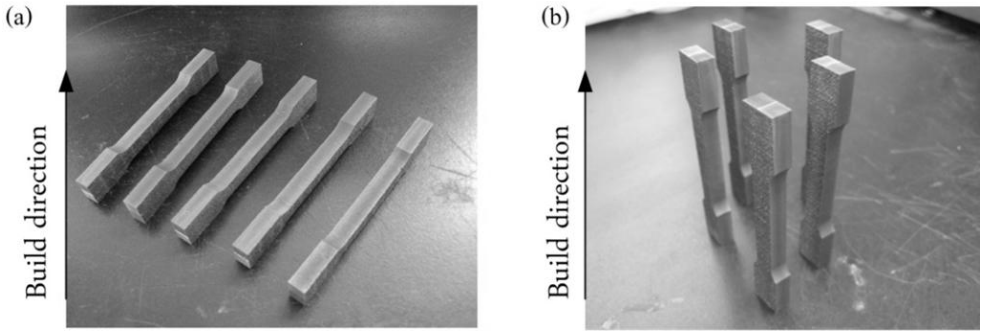

Figure 3.17: Tensile parts manufactured in case (a) part were build along transversal direction and case (b) part were build along longitudinal direction.

Table 3.4 Mechanical properties of SLM stainless steels pasts

Case of building parts	**Yield strength (MPa)**	**Ultimate tensile strength (MPa)**	**Elongation (%)**
a	313	474	5
b	265	474	12

It is obvious from Table 3.4 that the direction of processing parts is influenced on mechanical properties of specimen. The tensile property is measured in the direction perpendicular to the tensile axis, case (a), is expected to be higher than that parallel to the tensile axis, case (b). In this result, the yield strength of case (a) is indeed higher than case (b), whereas case (a) has percent elongation lower than case (b). It is explained by the fact that this experiment was tested under room temperature and the scanning area of each layer in case (a) was larger than case (b). It is possible that temperature variation in case (a) is higher than that in case (b) and thus the time-varying processing temperatures in case (a) results in higher internal stresses than that in case (b). The internal stress has an effect on mechanical property of the parts. On the other hand, an insufficient power of continue wave mode (CW) scanning can

cause the pore within the part and the bad interlayer connection. However, these problems may overcome by preheating and heating treatment the parts (Peter and Jean-Pierre, 2006; Shiomi et al., 2004)

As compared to the ASTM A240/A240M-04 (standard properties of 316L stainless steel rolled parts), the yield strength of the obtained SLM parts from this experiment is higher and tensile strength is closed to σ_u of standard property (Figure 3.18). That yield strength of SLM part is higher than that of the standard property and tensile strength of SLM parts is closed to σ_u of standard property. However, the percent elongation of SLM parts is lower than that of the standard property. This can explain that elongation of SLM parts is due to the fine grain structure of SLM parts as shown in Figure 3.19(b). This grain structure can cause brittlement in material and facilitating crack formation. Kruth et al., 2004 investigated the mechanical values of SLM SS 316L[a] and they found that the results were comparable to bulk material apart from the ductility, which was strongly reduced (See Table 3.5). This can be overcome by applying the right heat treatment. In addition they suggested that the temperature variation of the part can be minimized by heating the base plate, or even using pulse mode scanned instead of CW mode to avoid an insufficient power.

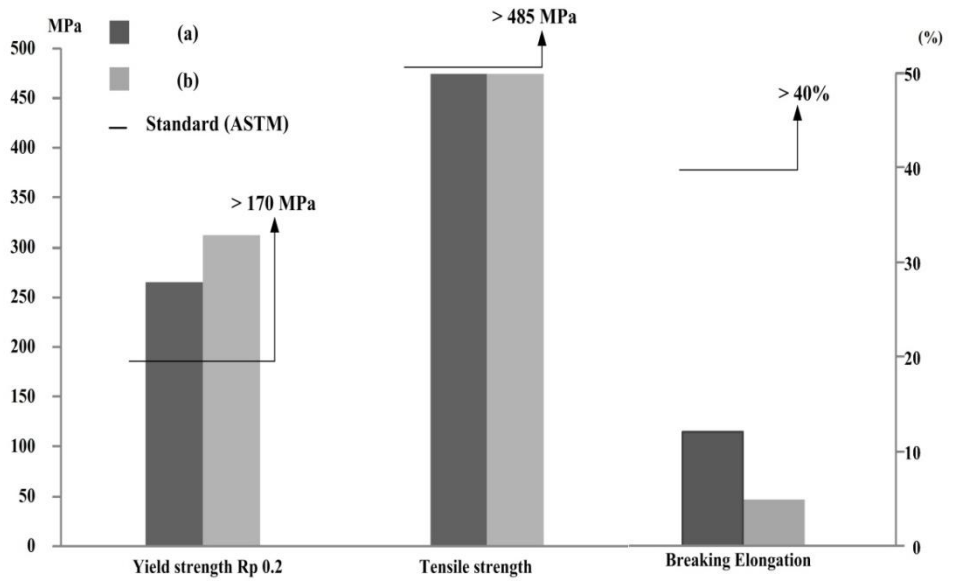

Figure 3.18: Comparison of SLM part properties and standard properties.

Table 3.5 Comparison of mechanical properties between SLM process and conventional process 316L stainless steels

Mechanical properties	Standard (ASTM)	SLM SS 316L[a]	SLM SS 316L[b]
Tensile strength (MPa)	485	480-520	474
Yield strength (MPa)	170	420-475	313
Elongation (%)	40	10-15	12
Hardness	228 HV	220-250 HV	228 HV
Density (%)	ca. 100	ca. 100	ca. 98.7

Source: [a] Kruth et al. 2005 and [b] The optimum conditions of this study

3.4 Microstructure analysis

The cross-section of parts processed with the optimal condition for multiple layers scanning were prepared for microstructure observation. From Figure 3.19(a), the pores inside the sample are indicated. Creation of pore in the parts are known as a result from the melting and solidification phenomena and also regarding insufficient surface quality as the roughness surface is high, greater possibility to entrap the gas upon deposition of a new powder layer and thus creating a pore. Fine cellular-dendrite grains with less than l μm grain of SLM part is shown in Figure 3.19(b). It has been noted that formation of fine cellular-dendrite grains with different grain growth directions resulted of a rapid solidification in SLM process and the difference of the cooling directions in the melt pool. Kruth et al., 2010 reported that the cellular-dendrite structure was more apparent in the laser re-molten zone than in the lower layers that were not re-melted and the cell size found to be finer in laser surface re-melting microstructures. It was equiaxed and homogenously visible throughout the re-molten zone or overlapping zone. Kumar, 2008 found that the SLM part appeared dendrites microstructure by the grain an average size of 10-15 μm. The dendrites structure was the prevalence microstructure of steel-based powders fabricated by SLM however, it can be minimized by optimization of the process parameters (Kumar 2008; Tolosa et al. 2010).

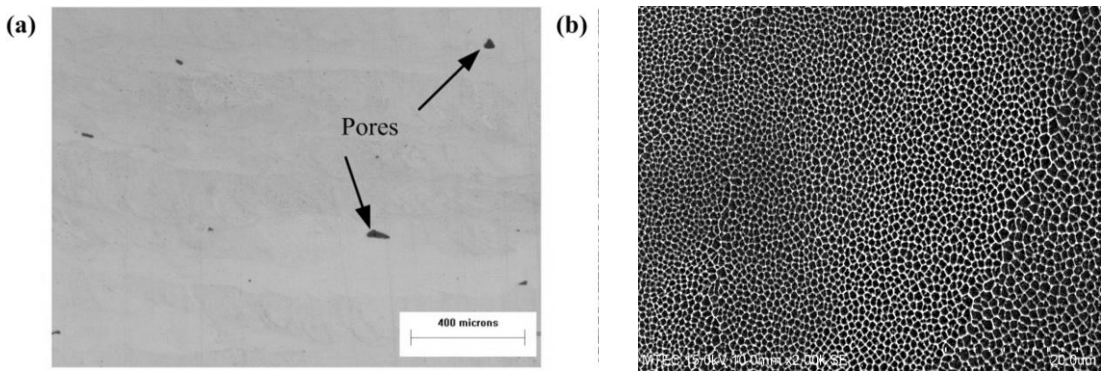

Figure 3.19 Microstructure from cross section view of 316L stainless steel fabricated by SLM technique: (a) optical micrograph showing pores in the 98.6% dense specimen and (b) SEM micrograph showing typical fine rapid solidified microstructure.

3.5 Electron probe micro-analysis (EPMA)

EPMA line scanning mode was utilized to examine the elemental distribution of the SLM parts. Elemental line scan analyses were carried out on the surface along the red arrow-marked direction, as illustrated in Figure 3.2 (a) and (b) shown features of surface. The results from EPMA line scans (Figure 3.20 (c)) indicated that Fe and Cr were two major elements and other elements were Mn, Mo, C, P, O, Si, S, N and Ni containing in the part of 316L stainless steel. Therefore, it could be concluded that 316L stainless steel SLM processed specimen had homogeneous chemical composition.

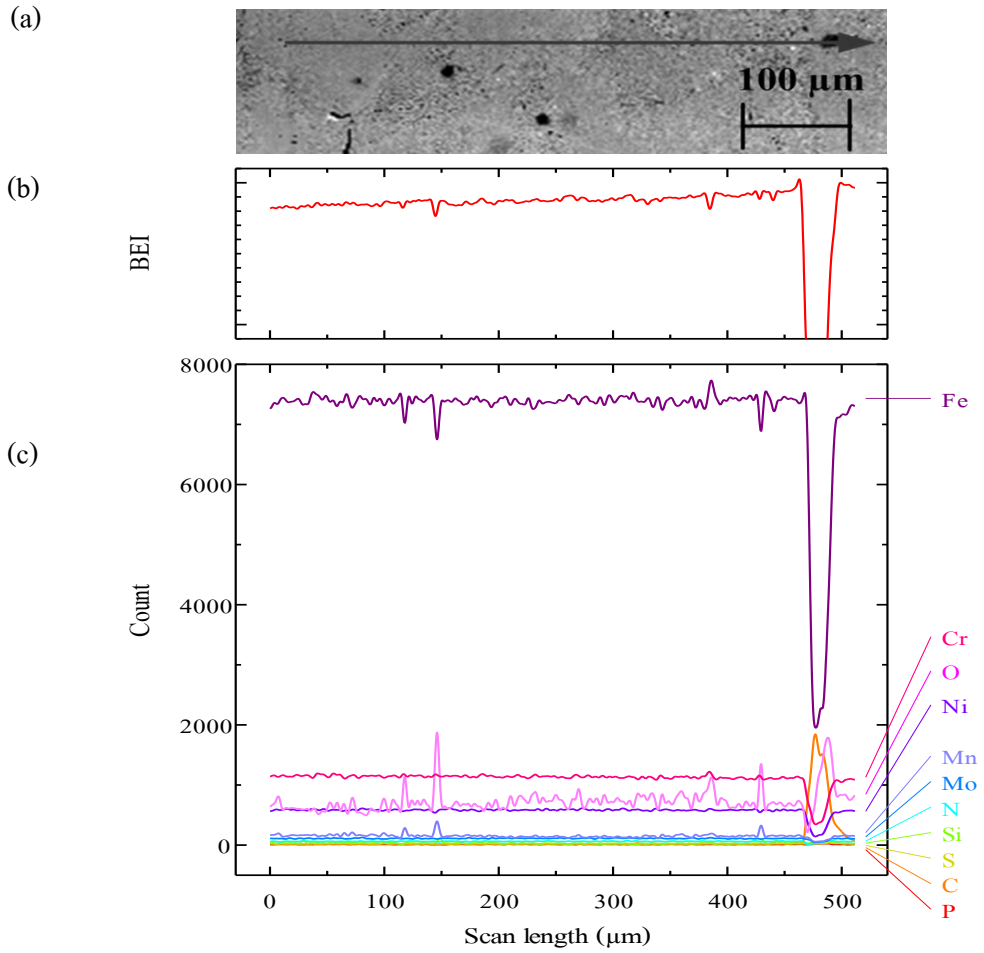

Figure 3.20: EPMA micrographs and EPMA line scanning profile of 316L stainless steel parts, (a) micrographs of on surface, (b) features on surface and (c) EPMA line scanning.

CHAPTER 4

Conclusions

4.1 Conclusions

4.1.1 Optimization SLM Process

Single line scanning was produced at various laser power and scan speed. The line tracks were identified into 5 zones including un-melt, over-melt, balling, irregular and smooth track. The track zone achieved from testing with laser power and scan speed in the approximately range of 75-175 W and 80-200 mm/s, respectively.

On performing the 2^4 factorial designs of experiment found that the parameters in this process not depends only on the individual parameters settings but also on the interactions and combination of fabrication parameters. The decreasing in part density led to decreasing in its hardness. Consequently, it was concluded that laser power, scan speed, scan spacing and scan strategy had significant effect on part's density and hardness. But laser power and scan strategy had insignificant effect on build rate. Moreover, it can be concluded that the optimum condition for processing multi-layers part was at a laser power of 175 W, a scan speed of 200 mm/s, a scan spacing of 0.04 mm and a scan strategy of 5 mm (sub-sector). This condition can fabricate parts, which appeared density 98.6%, hardness 228 HV and build rate 1.87 cm^3/hr.

4.1.2 Mechanical properties

The optimal part had the hardness and the yield strength values of 228 HV and 313 MPa respectively which were clearly higher than the standard properties. The ultimate tensile strength of the part was 474 MPa which was closed to standard property while the elongation was about 12 % which was lower than standard property. However, it

was proved in the literature that the mechanical properties of SLM part can be improved by preheating and heat treating. Besides, the mechanical properties of SLM part were classified in two different orientations. It appeared to be anisotropy properties.

From microstructure observation, the SLM part showed cellular-dendrite structure with less than l μm grain size which cause SLM part brittle than standard part. This research suggested that the formation of satisfied 316L parts from powder can be controlled by the adjustments of laser power, scan speed, scan spacing and scan strategy to reach optimum conditions. The SLM process holds high potential for the production of fully functional high density components in a single step as well as the possibility of fabricating functionally graded parts.

4.2 Suggestions

4.2.1 Oxygen level in the processing chamber

The SLM of metal powders is often accompanied by oxidation due to the presence of oxygen in the processing chamber. Therefore, the chamber should be designed to control the oxygen level at least be lower than 0.3 % (Van Elsen et al., 2007). This is done by flushing inert gas into the chamber and processing at atmospheric pressure.

4.2.2 Preheating

Preheating of the process chamber can be applied with the available equipment. Practically, the preheating temperature is performed in range of 25˚C-250˚C (Van Elsen et al., 2007) to reduce the residual thermal stresses in the final part. Nevertheless, high preheating temperature should be limited to avoid solid state sintering and to avoid thermal deviations of the optical system.

4.2.3 Scan strategy

The scan strategy is used to fill a large cross-section with scan tracks. The cross-section should be subdivided into quadrants and sectors (smaller areas) since this can reduce the different temperature in the part and then decrease the residual stress in final part.

4.3 Suggestions for further research

The presented research is far from finished. Here are two suggestions for further research, being a direct continuation of the presented work.

- **Optimization of composite materials:** It is possible to build the SLM part using composite materials since it is interest from many industrial applications.
- **Optimization of overhanging structures**: The study on overhanging structures proved that it is feasible to extend the possibilities of the process by changing the process parameters during the process. The irregularities of on the edges could be improved. The effect of the length of the scan tracks could be investigated. The repeatability can be studied and the feedback could be used.

REFERENCES

Annual book of ASTM standards. 2005. Iron and steel products. In *Steel-Plate, Sheet, Strip, Wire; Stainless steel bar*: ASTM International.

ASM Handbook Volume 09: Metallography and Microstructures.

Ben, Vandenbroucke. 2008. Selective laser melting of biocompatible metals for rapid manufacturing of medical parts, Faculteit Ingenieurswetenschappen, Departement Werktuigkunde K.U.Leuven.

Ben, Vandenbroucke, and Kruth Jean-Pierre. 2007. Selective laser melting of biocompatible metals for rapid manufacturing of medical parts. *Rapid Prototyping Journal* 13 (4):196-203.

Childs, T. H. C., C. Hauser, and M. Badrossamay. 2004. Mapping and Modelling Single Scan Track Formation in Direct Metal Selective Laser Melting. *CIRP Annals - Manufacturing Technology* 53 (1):191-194.

Dingal S., Pradhan T. R., Sundar S., Choudhury A. R., and Roy S. K. 2004. Experimental investigation of selective laser sintering of iron powder by application of Taguchi method. In Proc. of the 4th Laser Assisted Net Shape Engineering (LANE) Conference, pages 445 – 456.

Eustathopoulos, N., M.G. Nicholas, and B. Drevet. 1999. *Wettability at high temperatures*, *Pergamom materials series*.

Gu, Dongdong, and Yifu Shen. 2009. Balling phenomena in direct laser sintering of stainless steel powder: Metallurgical mechanisms and control methods. *Materials & Design* 30 (8):2903-2910.

Gusarov, A. V., I. Yadroitsev, Ph Bertrand, and I. Smurov. 2007. Heat transfer modelling and stability analysis of selective laser melting. *Applied Surface Science* 254 (4):975-979.

Hao, L., S. Dadbakhsh, O. Seaman, and M. Felstead. 2009. Selective laser melting of a stainless steel and hydroxyapatite composite for load-bearing implant development. *Journal of Materials Processing Technology* 209 (17):5793-5801.

Hauser, C., T. H. C. Childs, K. W. Dalgarno, and Eane R.B. 1999. Atmospheric control during selective laser sintering of stainless steel 314S Paper read at Proceeding of the solid freeform fabrication symposium.

Joo, Byeong-Don, Jeong-Hwan Jang, Jae-Ho Lee, Young-Myung Son, and Young-Hoon Moon. 2009. Selective laser melting of Fe-Ni-Cr layer on AISI H13 tool steel. *Transactions of Nonferrous Metals Society of China* 19 (4):921-924.

Kamran, Mumtaz, and Hopkinson Neil. 2009. Top surface and side roughness of Inconel 625 parts processed using selective laser melting. *Rapid Prototyping Journal* 15 (2):96-103.

Khan, Mushtaq, and Phill Dickens. 2010. Selective laser melting of pure gold. *Gold bulletin* 43 (2):114-121.

Kruth, J. P., M. Badrossamay, E. Yasa, L. Thijs, and J. Van Humbeeck. 2010. Part and material properties in selective laser melting of metals. Paper read at Proceedings of the 16th International Symposium on Electromachining.

Kruth, J. P., L. Froyen, J. Van Vaerenbergh, P. Mercelis, M. Rombouts, and B. Lauwers. 2004. Selective laser melting of iron-based powder. *Journal of Materials Processing Technology* 149 (1-3):616-622.

Kruth, J. P., M. C. Leu, and T. Nakagawa. 1998. Progress in additive manufacturing and rapid prototyping. *CIRP Annals - Manufacturing Technology* 47 (2):525-540.

Kruth, J. P., G. Levy, F. Klocke, and T. H. C. Childs. 2007. Consolidation phenomena in laser and powder-bed based layered manufacturing. *CIRP Annals - Manufacturing Technology* 56 (2):730-759.

Kruth, J. P., P. Mercelis, J. Van Vaerenbergh, L. Froyen, and M. Rombouts. 2005. Binding mechanisms in selective laser sintering and selective laser melting. *Rapid Prototyping Journal* 11 (1):26-36.

Kumar, S. 2008. Microstructure and wear of SLM materials. *Advanced engineering materials* 10 (8).

Li, Ruidi, Yusheng Shi, Zhigang Wang, Li Wang, Jinhui Liu, and Wei Jiang. 2010. Densification behavior of gas and water atomized 316L stainless steel powder during selective laser melting. *Applied Surface Science* 256 (13):4350-4356.

Matsumoto, M., M. Shiomi, K. Osakada, and F. Abe. 2002. Finite element analysis of single layer forming on metallic powder bed in rapid prototyping by selective laser processing. *International Journal of Machine Tools and Manufacture* 42 (1):61-67.

Mills, K.C., B.J. Keene, R.F. Brooks, and A. Shirali. 1998. Marangoni effects in welding. *Phil. Trans. R. Soc, Lond. A* 356:911-925.

Montgomery, Douglas C. 1991. The 2k factorial design. In *Design and analysis of experiments (Third edition)*. Singapore: John wiley & Sons.

Morgan, R., C. J. Sutcliffe, and W. O'Neill. 2001. Experimental investigation of nanosecond pulsed Nd:YAG laser re-melted pre-placed powder beds. *Rapid Prototyping Journal* 7 (3):159-172.

Morgan, R., C. J. Sutcliffe, and W. O'Neill. 2004. Density analysis of direct metal laser re-melted 316L stainless steel cubic primitives. *Materials Science Journal* (39): 1195-1205.

Mumtaz, Kamran Aamir, Poonjolai Erasenthiran, and Neil Hopkinson. 2008. High density selective laser melting of Waspaloy. *Journal of Materials Processing Technology* 195 (1-3):77-87.

Osakada, Kozo, and Masanori Shiomi. 2006. Flexible manufacturing of metallic products by selective laser melting of powder. *International Journal of Machine Tools and Manufacture* 46 (11):1188-1193.

Peter, Mercelis, and Kruth Jean-Pierre. 2006. Residual stresses in selective laser sintering and selective laser melting. *Rapid Prototyping Journal* 12 (5):254-265.

Pham, D. T., and R. S. Gault. 1998. A comparison of rapid prototyping technologies. *International Journal of Machine Tools and Manufacture* 38 (10-11):1257-1287.

Rombouts, M. 2006. Selective laser sintering/melting of iron-based powders, Ph.D. in Materials Engineering Katholieke Uinversiteit, Leuven.

Rombouts, M., J. P. Kruth, L. Froyen, and P. Mercelis. 2006. Fundamentals of Selective Laser Melting of alloyed steel powders. *CIRP Annals - Manufacturing Technology* 55 (1):187-192.

Santos, Edson Costa, Masanari Shiomi, Kozo Osakada, and Tahar Laoui. 2006. Rapid manufacturing of metal components by laser forming. *International Journal of Machine Tools and Manufacture* 46 (12-13):1459-1468.

Shiomi, M., K. Osakada, K. Nakamura, T. Yamashita, and F. Abe. 2004. Residual Stress within Metallic Model Made by Selective Laser Melting Process. *CIRP Annals - Manufacturing Technology* 53 (1):195-198.

Simchi, A. 2004. The role of particle size on the laser sintering of iron powder. *Metallurgical and Materials Transactions B* 35 (5):937-948.

Sung-Hoon, Ahn, Montero Michael, Odell Dan, Roundy Shad, and K. Wright Paul. 2002. Anisotropic material properties of fused deposition modeling ABS. *Rapid Prototyping Journal* 8 (4):248-257.

Tolosa, Itziar, Fermín Garciandía, Fidel Zubiri, Fidel Zapirain, and Aritz Esnaola 2010. Study of mechanical properties of AISI 316 stainless steel processed by "selective laser melting", following different manufacturing strategies. *The International Journal of Advanced Manufacturing Technology* 51 (5):639-647.

Van Elsen, M. 2007. Complexity of selective laser melting: a new optimisation approach, Machanical engineering, Katholieke Universiteit Leuven.

Van Elsen, M., M. Baelmans, P. Mercelis, and J. P. Kruth. 2007. Solutions for modelling moving heat sources in a semi-infinite medium and applications to laser material processing. *International Journal of Heat and Mass Transfer* 50 (23-24):4872-4882.

Wohlers, Terry T. 2009. *Wohlers State of the industry, Annual worldwide progress report*: Wholers associates.

Yadroitsev, I., Ph Bertrand, and I. Smurov. 2007. Parametric analysis of the selective laser melting process. *Applied Surface Science* 253 (19):8064-8069.

Yadroitsev, I., A. Gusarov, I. Yadroitsava, and I. Smurov. Single track formation in selective laser melting of metal powders. *Journal of Materials Processing Technology* 210 (12):1624-1631.

Zhang, Wenxian, Yusheng Shi, Bing Liu, Lin Xu, and Wei Jiang. 2009. Consecutive sub-sector scan mode with adjustable scan lengths for selective laser melting technology. *The International Journal of Advanced Manufacturing Technology* 41 (7):706-713.

Standard test method for Viker Indentation hardness of advanced ceramics. In ASTM standard C1327-03.2005.

Standard test methods for tension testing metallic materials. In ASTM standard E8M-00a.2005.

Standard test methods for density determination for power metallurgy (P/M) materials containing less than two percent porosity. In ASTM B 311-93.2005.

APPENDIX A

Appendices A

A1. Data of multi-layer scanning

No	Parameters	Replicate	Density (%)	Average (%)	Build rate (cm^3/hr)
1	P 75 W, V 200 mm/s	1	80.0300	**80.39**	**1.85**
	Ss 0.04 mm, S 10 mm	2	80.7662		
2	P 175 W, V 200 mm/s	1	97.7459	**97.57**	**1.85**
	Ss 0.04 mm, S 10 mm	2	97.3993		
3	P 75 W, V 200 mm/s	1	88.0937	**87.98**	**1.87**
	Ss 0.04 mm, S 5 mm	2	87.8692		
4	P 175 W, V 200 mm/s	1	98.4267	**98.50**	**1.87**
	Ss 0.04 mm, S 5 mm	2	98.5990		
5	P 75 W, V 80 mm/s	1	89.5218	**89.29**	**0.93**
	Ss 0.04 mm, S 10 mm	2	89.0646		
6	P 175 W, V 80 mm/s	1	98.7076	**98.50**	**0.93**
	Ss 0.04 mm, S 10 mm	2	98.3092		
7	P 75 W, V 80 mm/s	1	94.3602	**94.29**	**0.95**
	Ss 0.04 mm, S 5 mm	2	94.2323		
8	P 175 W, V 80 mm/s	1	98.3400	**98.30**	**0.95**
	Ss 0.04 mm, S 5 mm	2	98.2600		
9	P 75 W, V 200 mm/s	1	81.9186	**81.64**	**2.58**
	Ss 0.06 mm, S 10 mm	2	81.3747		
10	P 175 W, V 200 mm/s	1	88.9292	**88.70**	**2.58**
	Ss 0.06 mm, S 10 mm	2	88.4716		
11	P 75 W, V 200 mm/s	1	85.7689	**85.70**	**2.39**
	Ss 0.06 mm, S 5x5 mm	2	85.6402		
12	P 175 W, V 200 mm/s	1	97.3523	**97.37**	**2.39**
	Ss 0.06 mm, S 5x5 mm	2	97.3966		
13	P 75 W, V 80 mm/s	1	89.5825	**88.47**	**1.47**
	Ss 0.06 mm, S 10 mm	2	89.4818		
14	P 175 W, V 80 mm/s	1	97.8669	**97.81**	**1.47**
	Ss 0.06 mm, S 10 mm	2	97.7622		
15	P 75 W, V 80 mm/s	1	93.3092	**92.68**	**1.50**
	Ss 0.06 mm, S 5x5 mm	2	92.0678		
16	P 175 W, V 80 mm/s	1	97.7919	**97.80**	**1.50**
	Ss 0.06 mm, S 5x5 mm	2	97.8123		

A2. Hardness test results

No	Parameters	Rep.	HV1	HV2	HV3	HV4	HV5	HV6	HV7	HV8	HV9	SD.	Avg.1 (HV)	Avg.2 (HV)
1	P 75 W, V 200 mm/s	1	205.55	206.69	205.59	214.90	198.91	211.32	208.98	214.90	208.98	5.0336	208.42	**208.44**
	Ss 0.04 mm, S 10 mm	2	210.15	208.98	203.31	199.62	219.84	202.33	213.86	205.55	212.50	6.4112	208.46	
2	P 175 W, V 200 mm/s	1	213.96	216.11	216.11	218.60	219.81	227.50	219.90	224.93	218.56	4.3173	219.50	**219.68**
	Ss 0.04 mm, S 10 mm	2	217.87	219.81	222.33	228.82	222.29	215.15	219.33	212.50	220.69	4.6580	219.87	
3	P 75 W, V 200 mm/s	1	204.71	219.84	214.85	206.81	216.11	202.50	214.90	217.29	212.33	6.0530	212.15	**211.92**
	Ss 0.04 mm, S 5 mm	2	212.50	216.11	208.82	209.81	214.93	218.53	202.33	216.11	206.23	5.3174	211.71	
4	P 175 W, V 200 mm/s	1	227.46	224.53	229.46	236.99	227.50	225.81	232.90	225.28	232.23	4.1558	229.13	**228.41**
	Ss 0.04 mm, S 5 mm	2	226.25	229.36	218.56	222.36	236.99	234.42	225.15	226.56	229.69	5.7024	227.70	
5	P 75 W, V 80 mm/s	1	207.83	206.69	213.69	209.81	218.56	212.50	198.61	204.67	202.74	6.0727	208.34	**208.65**
	Ss 0.04 mm, S 10 mm	2	212.50	216.11	200.99	209.61	208.82	207.83	216.11	206.69	202.04	5.3974	208.97	
6	P 175 W, V 80 mm/s	1	221.32	218.98	223.95	235.55	225.90	227.83	232.50	227.83	235.05	5.8390	227.66	**227.95**
	Ss 0.04 mm, S 10 mm	2	228.23	225.69	230.81	232.29	229.50	221.15	227.83	232.69	226.11	3.6378	228.26	
7	P 75 W, V 80 mm/s	1	214.90	216.19	212.5	214.85	213.69	217.33	208.53	217.84	211.49	2.9694	214.15	**213.72**
	Ss 0.04 mm, S 5 mm	2	213.15	215.64	211.32	215.05	210.15	221.28	208.91	214.22	209.99	3.8269	213.30	
8	P 175 W, V 80 mm/s	1	220.46	221.14	218.56	226.11	221.10	232.50	237.83	230.07	228.82	6.5159	226.29	**225.75**
	Ss 0.04 mm, S 5 mm	2	223.69	220.11	233.28	217.93	229.82	227.50	220.99	223.62	229.98	5.1965	225.21	
9	P 75 W, V 200 mm/s	1	197.87	206.72	192.64	208.82	202.50	198.76	207.83	208.83	205.76	5.7412	203.30	**202.65**
	Ss 0.06 mm, S 10 mm	2	193.71	203.56	194.71	196.62	208.33	206.69	197.67	206.70	210.15	6.3499	202.02	
10	P 175 W, V 200 mm/s	1	216.11	223.56	216.69	212.33	210.15	216.11	217.99	219.81	212.50	4.1216	216.14	**216.04**
	Ss 0.06 mm, S 10 mm	2	214.64	217.33	219.81	213.56	207.33	217.35	221.06	217.50	214.90	4.0329	215.94	

A3. Hardness test results (continued)

No.	Parameters	Rep.	HV1	HV2	HV3	HV4	HV5	HV6	HV7	HV8	HV9	SD.	Avg.1 (HV)	Avg.2 (HV)
11	P 75 W, V 200 mm/s	1	207.83	206.78	210.91	208.98	198.67	209.67	213.64	216.11	208.43	4.8671	209.00	**209.45**
	Ss 0.06 mm, S 5x5 mm	2	211.32	202.42	213.69	207.50	210.81	200.91	211.32	212.69	218.54	5.5248	209.91	
12	P 175 W, V 200 mm/s	1	212.50	228.28	223.15	224.90	229.56	228.90	220.50	219.12	224.46	5.4877	223.49	**223.00**
	Ss 0.06 mm, S 5x5 mm	2	217.50	215.15	220.11	228.56	225.83	225.90	227.83	222.58	219.31	4.7787	222.53	
13	P 75 W, V 80 mm/s	1	216.11	217.33	201.06	213.64	219.77	206.23	220.82	217.50	217.10	6.5550	214.40	**214.77**
	Ss 0.06 mm, S 10 mm	2	212.36	214.90	227.50	211.06	218.60	211.10	216.14	219.81	204.89	6.4553	215.15	
14	P 175 W, V 80 mm/s	1	222.29	227.46	219.81	234.22	231.49	223.64	224.85	224.89	228.82	4.5642	226.39	**226.67**
	Ss 0.06 mm, S 10 mm	2	227.46	221.02	232.85	235.60	221.06	223.56	226.11	224.85	230.15	5.0818	226.96	
15	P 75 W, V 80 mm/s	1	208.98	211.32	218.69	208.98	214.69	215.55	219.32	214.90	220.33	4.2802	214.75	**214.59**
	Ss 0.06 mm, S 5x5 mm	2	204.43	218.98	210.28	213.69	217.33	218.69	215.55	214.90	216.11	4.6006	214.44	
16	P 175 W, V 80 mm/s	1	218.69	220.15	219.84	223.90	216.11	228.50	216.69	229.81	224.89	4.9637	222.06	**221.69**
	Ss 0.06 mm, S 5x5 mm	2	225.15	217.83	209.53	224.93	226.11	223.50	227.46	221.69	215.81	5.8606	221.33	

A4. Tensile test results (Case a)

No.	Max load(kN)	Tensile stress at yield (offet 0.2%) (MPa)	Maximum tensile strength (MPa)	Modulus (AutomaticYoung's) (MPa)	Tensile strain at break (%)
1	15.57	294.24	505.71	62,669	6.4
2	14.88	305.14	471.05	55,963	5.61
3	15.19	326.78	469.31	68,640	5.02
4	14.67	326.94	450.3	62,224	4.48
Avg.		313.275	474.0925	62,374	5.3775

A5. Tensile test results (Case b)

No.	Max load (kN)	Tensile stress at yield (offet 0.2%) (MPa)	Maximum tensile strength (MPa)	Modulus (AutomaticYoung's) (MPa)	Tensile strain at break (%)
1	15.78	274.37	480.14	49,287	12.9
2	15.20	260.31	467.18	70,227	10.88
3	14.57	256.62	465.85	71,345	10.8
4	14.83	266.89	481.69	57,619	12.26
Avg.		264.5475	473.72	62,120	11.71

A6. General linear model: Density

Factor **Type** **Levels** **Values**
Laser power **fixed** **2** **75, 175**
Scan speed **fixed** **2** **80, 200**
Scan spacing **fixed** **2** **0.04, 0.06**
Scan strategy **fixed** **2** **5, 10**

Analysis of Variance for Density (%), using Adjusted SS for Tests

Source	**DF**	**Seq SS**	**Adj SS**	**Adj MS**	**F**	**P**
Laser power	1	650.342	650.342	650.342	401.70	0.000
Scan speed	1	149.126	149.126	149.126	92.11	0.000
Scan spacing	1	12.575	12.575	12.575	7.77	0.013
Scan strategy	1	76.694	76.694	76.694	47.37	0.000
Laser power*Scan speed	1	50.803	50.803	50.803	31.38	0.000
Laser power*Scan spacing	1	36.594	36.594	36.594	22.60	0.000
Laser power*Scan strategy	1	5.330	5.330	5.330	3.29	0.088
Scan speed*Scan spacing	1	1.656	1.656	1.656	1.02	0.327
Scan speed*Scan strategy	1	36.808	36.808	36.808	22.74	0.000
Scan spacing*Scan strategy	1	3.605	3.605	3.605	2.23	0.155
Laser power*Scan speed* Scan spacing	1	4.176	4.176	4.176	2.58	0.128
Laser power*Scan speed* Scan strategy	1	6.552	6.552	6.552	4.05	0.061
Laser power*Scan spacing* Scan strategy	1	2.409	2.409	2.409	1.49	0.240
Scan speed*Scan spacing* Scan strategy	1	24.992	24.992	24.992	15.44	0.001
Laser power*Scan speed* Scan spacing*Scan strategy	1	13.886	13.886	13.886	8.58	0.010
Error	16	25.903	25.903	1.619		
Total	31	1101.454				

S = 1.27238 **R-Sq = 97.65%** **R-Sq(adj) = 95.44%**

Term	**Coef**	**SE Coef**	**T**
Constant	92.1931	0.2249	409.88
Laser power			
75	-4.5081	0.2249	-20.04
Scan speed			
80	2.1588	0.2249	9.60
Scan spacing			
0.04	0.6269	0.2249	2.79
Scan strategy			
5	1.5481	0.2249	6.88
Laser power*Scan speed			
75 80	1.2600	0.2249	5.60
Laser power*Scan spacing			
75 0.04	-1.0694	0.2249	-4.75
Laser power*Scan strategy			
75 5	0.4081	0.2249	1.81
Scan speed*Scan spacing			
80 0.04	-0.2275	0.2249	-1.01
Scan speed*Scan strategy			
80 5	-1.0725	0.2249	-4.77
Scan spacing*Scan strategy			

```
0.04          5                                      -0.3356   0.2249   -1.49
Laser power*Scan speed*Scan spacing
 75          80          0.04                         0.3612   0.2249    1.61
Laser power*Scan speed*Scan strategy
 75          80           5                           0.4525   0.2249    2.01
Laser power*Scan spacing*Scan strategy
 75         0.04          5                           0.2744   0.2249    1.22
Scan speed*Scan spacing*Scan strategy
 80          0.04          5                          0.8837   0.2249    3.93
Laser power*Scan speed*Scan spacing*Scan strategy
 75          80          0.04          5             -0.6588   0.2249   -2.93
```

A7. General linear model: Hardness

Factor	**Type**	**Levels**	**Values**
Laser power	**fixed**	**2**	**75, 175**
Scan speed	**fixed**	**2**	**80, 200**
Scan spacing	**fixed**	**2**	**0.04, 0.06**
Scan strategy	**fixed**	**2**	**5, 10**

Analysis of Variance for Hardness (HV), using Adjusted SS for Tests

Source	**DF**	**Seq SS**	**Adj SS**	**Adj MS**	**F**	**P**
Laser power	1	1377.99	1377.99	1377.99	4424.05	0.000
Scan speed	1	146.16	146.16	146.16	469.25	0.000
Scan spacing	1	30.63	30.63	30.63	98.35	0.000
Scan strategy	1	70.12	70.12	70.12	225.13	0.000
Laser power*Scan speed	1	2.35	2.35	2.35	7.54	0.014
Laser power*Scan spacing	1	21.53	21.53	21.53	69.13	0.000
Laser power*Scan strategy	1	5.55	5.55	5.55	17.83	0.001
Scan speed*Scan spacing	1	44.91	44.91	44.91	144.19	0.000
Scan speed*Scan strategy	1	100.01	100.01	100.01	321.07	0.000
Scan spacing*Scan strategy	1	5.24	5.24	5.24	16.83	0.001
Laser power*Scan speed* Scan spacing	1	16.63	16.63	16.63	53.40	0.000
Laser power*Scan speed* Scan strategy	1	38.26	38.26	38.26	122.83	0.000
Laser power*Scan spacing* Scan strategy	1	0.84	0.84	0.84	2.68	0.121
Scan speed*Scan spacing* Scan strategy	1	11.44	11.44	11.44	36.72	0.000
Laser power*Scan speed* Scan spacing*Scan strategy	1	7.12	7.12	7.12	22.85	0.000
Error	16	4.98	4.98	0.31		
Total	31	1883.77				

S = 0.558102 R-Sq = 99.74% R-Sq(adj) = 99.49%

Term	**Coef**	**SE Coef**	**T**
Constant	217.092	0.099	2200.41
Laser power			
75	-6.56219	0.09866	-66.51
Scan speed			

```
 80                                                2.13719  0.09866    21.66
Scan spacing
0.04                                               0.97844  0.09866     9.92
Scan strategy
 5                                                 1.48031  0.09866    15.00
Laser power*Scan speed
 75          80                                    0.27094  0.09866     2.75
Laser power*Scan spacing
 75         0.04                                  -0.82031  0.09866    -8.31
Laser power*Scan strategy
 75          5                                     0.41656  0.09866     4.22
Scan speed*Scan spacing
 80          0.04                                 -1.18469  0.09866   -12.01
Scan speed*Scan strategy
 80           5                                   -1.76781  0.09866   -17.92
Scan spacing*Scan strategy
0.04          5                                    0.40469  0.09866     4.10
Laser power*Scan speed*Scan spacing
 75          80          0.04                     -0.72094  0.09866    -7.31
Laser power*Scan speed*Scan strategy
 75          80           5                       1.09344  0.09866    11.08
Laser power*Scan spacing*Scan strategy
 75         0.04          5                      -0.16156  0.09866    -1.64
Scan speed*Scan spacing*Scan strategy
 80          0.04          5                      0.59781  0.09866     6.06
Laser power*Scan speed*Scan spacing*Scan strategy
 75          80          0.04          5          0.47156  0.09866     4.78
```

A8. General linear model: Build rate

```
Factor          Type     Levels  Values
Scan speed      fixed       2     80, 200
Scan spacing    fixed       2   0.04, 0.06

Analysis of Variance for Build rate (cm^3/hr), using Adjusted SS for Tests

Source                          DF   Seq SS  Adj SS  Adj MS      F      P

Scan speed                       1   7.3728  7.3728  7.3728   2730.67  0.000
Scan spacing                     1   2.7378  2.7378  2.7378   1014.00  0.000
Scan speed*Scan spacing          1   0.0128  0.0128  0.0128      4.74  0.038
Error                           28   0.0756  0.0756  0.0027
Total                           31  10.1990


S = 0.0519615   R-Sq = 99.26%   R-Sq(adj) = 99.18%

Term                                        Coef   SE Coef       T      P

Constant                                 1.69250   0.00919  184.26   0.000
Scan speed
 80                                     -0.480000  0.009186  -52.26  0.000
Scan spacing
0.04                                    -0.292500  0.009186  -31.84  0.000
Scan speed*Scan spacing
 80          0.04                        0.020000  0.009186    2.18  0.038
```

A9. Response Optimization

Parameters

	Goal	Lower	Target	Upper	Weight	Import
Density(%)	Maximum	97.00	100.00	100.00	1	1
Hardness (HV)	Maximum	220.00	250.00	250.00	1	1
Build rate (cm^3/hr)	Maximum	0.93	2.58	2.58	1	1

Starting Point

laser power = 75
scan speed = 80
scan spacing = 0.04
scan strategy = 5

Global Solution

laser power = 175
scan speed = 200
scan spacing = 0.04
scan strategy = 5

Predicted Responses

Density(%) = 98.600 , desirability = 0.533333
Hardness (HV) = 228.417 , desirability = 0.280556
Build rate(cm^3/hr) = 1.870 , desirability = 0.569697

Composite Desirability = 0.440103

VITAE

Name Miss Apinya Laohaprapanon

Student ID 5210120046

Educational Attainment

Degree	Name of Institution	Year of Graduation
Bachelor of Engineering (Materials Engineering)	Prince of Songkla University	2009

Scholarship Awards during Enrolment

Thai Graduate Institute of Science and Technology

Work – Position and Address

Engineering 1 (Research and Development)

National metal and materials technology center

114 Thailand Science Park, Phahonyothin Rd. Klong 1, Klong Luang, Pathumthani 12120 Thailand.

List of Publication and Proceeding

- Laohaprapanon A., Chantarapanich N., Wisutmethangoon S., Jiamwatthanachai P., Chalermkarnnon P., Sucharitpwatskul S., Sitthiseripratip K., " Fabrication of Three-dimensional Honeycomb Structure for Aeronautical Applications using Selective Laser Melting: A Preliminary Investigation", submitted to Journal of rapid prototyping (2011).
- Laohaprapanon A., Jeamwatthanachai P., Wongcumchang M., Chantarapanich N., Chantaweroad S., Sitthiseripratip K., Wisutmethangoon S., "Optimal Scanning Condition of Selective Laser Melting Processing with Stainless Steel 316L Powder", International Conference on Material and Manufacturing Technology (ICMMT 2011), Xiamen, China. 8-10 July.